Ultra-peripheral J/ψ production in PbPb collisions at $\sqrt{s_{NN}}$=2.76 TeV with CMS

By

R. Patrick Kenny III

Submitted to the Department of People who read Abstracts and the
Graduate Faculty of the University of Kansas
in partial fulfillment of the requirements for the degree of
Doctor of Philosophy

	MEMBER 1, Chairperson
Committee members	MEMBER 2
	MEMBER 3
	MEMBER 4

Date defended: October 02, 2012

The Dissertation Committee for R. Patrick Kenny III certifies
that this is the approved version of the following dissertation :

Ultra-peripheral J/ψ production in PbPb collisions at $\sqrt{s_{NN}}$=2.76 TeV with CMS

____

MEMBER 1, Chairperson

Date approved: October 03, 2012

Abstract

The first is some LaTeX code, don't change it.

Acknowledgements

I would like to thank all of the little people who made this thesis possible.

Contents

List of Figures

List of Tables

Chapter 1

Introduction

1.1 Theoretical Context

1.2 History

Chapter 2

Theory

2.1 Introduction

Microseconds after the big bang, the universe existed in a state known as the Quark Gluon Plasma (QGP). In the QGP, quarks and gluons are not in hadronic bondage, forced to the confines of bound states such as protons and neutrons. The Large Hadron Collider (LHC) produces QGP in the lab in PbPb (lead-lead) collisions. The high energies and rates of the collisions at the LHC make it possible to do detailed studies of the QGP. The LHC is producing rare experimental probes such as suppressed jets and heavy quarkonia at an unprecedented rate in heavy-ion collisions. Physicists now have better constraints on the properties like temperature, viscosity, and energy density of the QGP.

The detailed studies of PbPb collisions coming out of the LHC experiments require an understanding of the initial state of the ions before they collide. Without knowledge of the initial state, physicists cannot determine which experimental effects are due to the QGP and which effects are inherent to the nuclei themselves. For example, suppression of heavy quarkonia is a signature of the QGP but also appears to occur in deuterium-gold collisions where the QGP is not expected to arise [2]. Because it is not certain how much of the reduction of quarkonia production is due to the initial state of the nuclei, the reduction due to the QGP is unclear. Without a clean probe of the initial state, physicists' knowledge of the QGP is limited. Ultra-Peripheral Collisions (UPC) at the LHC fill this need for a clean probe.

The colliding nuclei interact electromagnetically in an UPC event, avoiding the complicated mixing of final state and initial state effects found in nuclear collisions. In UPC events, no QGP state emerges, and the effects arising from the QGP no longer obscure the initial state effects. Other initial state probes such as peripheral nuclear collisions and proton-nucleus collisions have the potential to create the QGP obscuring which effects come from the initial state. It is impossible to create the QGP in UPC events because the nucleons within the nucleus do not collide. UPC events provide clarity by enhancing physicists' understanding of the initial state.

The interactions between the field of photons surrounding the colliding nuclei and the gluons of nuclei can produce a J/ψ probing the gluon density. The UPC J/ψ photoproduction cross section is therefore a probe of the initial state of the nucleus. The Weizsiäcker-Williams approximation provides a way to calculate the density of probing photons that surrounds the nucleus. The electron-proton scattering data gives a value for the proton photoproduction cross section at lower energies. The perterbutive Quantum Chromo-dynamics (pQCD), Vector Messon Dominance (VMD), and Leading Twist (LTA) methods all combined the nuclear photon flux with the proton scattering data to calculate the nuclear photoproduction cross section. Each of these methods handle the gluon density of the nucleus differently producing a measurable difference in the value of the J/ψ photoproduction cross section.

2.2 QCD/QGP

2.3 CGC/intial state

2.4 Weizsäcker-Williams Approximation

The Weizsiäcker-Williams approximation relates the electric field of a stationary point charge to the photon field that arises at ultra relativistic velocities. The approximation is semi-classical and combines both classical and quantum elements. A Fourier transform of Maxwell's equations combine with Einstein's equation for the energy of a photon in the Weizsiäcker-Williams approximation. The frequency modes of the electrostatic field are treated as photons. The conversion of the electric field to a flux of photons simplifies the calculation of interaction cross sections. The Weizsiäcker-Williams approximation makes the calculation of electromagnetic interactions with the nucleus tractable.

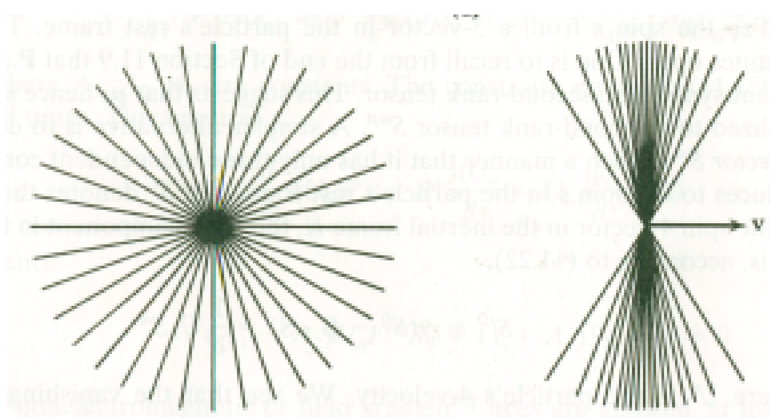

Figure 2.1: The electromagnetic field boosted and at rest.

The Wiezacker-Williams approximation begins with the equation for the electric field of the projectile nucleus at rest. The electromagnetic field only needs to be considered at the position of the target nucleus. From the projectile's point of view, the target is moving and contributes $-vt$ to

Eq. 2.1, the equation for the electric field of the projectile nucleus at rest.

$$x' = -vt' \qquad y' = b \qquad z' = 0 \qquad \vec{\mathbf{E}}' = \left(\frac{eZ}{4\pi\varepsilon_0 \left((-vt')^2 + b^2 \right)^{3/2}} \right) \left(-vt'\hat{\mathbf{x}}' + b\hat{\mathbf{y}}' \right) \tag{2.1}$$

In Eq. 2.1, b is the impact parameter, the distance of separation at closest approach, v is the velocity of the projectile nucleus, Z is the number of protons in the nucleus, and e is the charge of the electron. Two simplifications occur due to the coordinates of Eq. 2.1. The magnetic field is equal to zero, because the projectile is at rest, and the z coordinate can be ignored, reducing the equation to two dimensions.

The Lorentz transformation converts the field equations in the projectile's frame to equations in the target's frame. The result is a set of equations that relate the electric and magnetic field components in one frame to the components of the electric and magnetic field in another frame moving at a different constant velocity. Eq. 2.2 gives the result of the transformation from the projectile's primed frame to the target's rest frame for the field components [3]:

$$\begin{aligned} E'_x = E_x \qquad \gamma\left(E'_y/c + \beta B'_z\right) = E_y/c \qquad \gamma\left(E'_z/c = \beta B'_y\right) = E_z/c \\ B'_x = B_x \qquad \gamma\left(B'_y - \beta E'_z/c\right) = B_y \qquad \gamma\left(B'_z + \beta E'_y/c\right) = B_z \end{aligned} \tag{2.2}$$

The transformation equations for the fields, Eq. 2.2, and the transformation of the coordinates reduce to Eq. 2.3 [3]:

$$\begin{aligned} E'_x = E_x \qquad \gamma E'_y = E_y \qquad \gamma\beta E'_y/c = B_z \\ ct' = \gamma ct \qquad x' = -\gamma\beta ct \end{aligned} \tag{2.3}$$

The simplicity of Eq. 2.1 creates the simplicity of Eq. 2.2. The Lorentz transformation reduces the six components of the electromagnetic field in the target's frame to the three equations in Eq. 2.2 by relating them to the fields of the projectile's frame.

The combination of Eq. 2.1 and Eq. 2.2 produce equations for the electric and magnetic fields in the target's rest frame. Eq. 2.1 gives the expression for the field components as seen in the projectile frame.

$$\vec{\mathbf{E}} = \left(\frac{\gamma e Z}{4\pi\varepsilon_0 \left((\gamma v t)^2 + b^2 \right)^{3/2}} \right) (vt\hat{\mathbf{x}} + b\hat{\mathbf{y}})$$
$$\vec{\mathbf{B}} = \frac{\gamma\beta e Z b}{4\pi c\varepsilon_0 \left((\gamma v t)^2 + b^2 \right)^{3/2}} \hat{\mathbf{z}} = \frac{\gamma\mu_0 v e Z b}{4\pi \left((\gamma v t)^2 + b^2 \right)^{3/2}} \hat{\mathbf{z}} \tag{2.4}$$

If the impact parameter b goes to zero, the target sits in the line of the projectile particle's motion, and the denominator carries a factor of γ squared. If vt goes to zero, the projectile particle is directly above or below in the y direction, and the numerator carries a factor of γ. This results in fields that are a factor of γ^3 higher in the y direction than in the x direction (see Fig. 2.1). The boost compresses the electric field of the charge in the direction of the boost and produces a magnetic field resulting in a form similar to radiation. The point charge at ultra relativistic velocities produces a strong electric field in the plane transverse to its motion resembling a plane wave.

Separating the even and odd functions of the electromagnetic field simplify the decomposition of the field equations into Fourier modes. The even functions decompose into cosine functions, odd functions into sine functions. The y-component of the electric field and the z-component of the magnetic field are even functions in time, and the x-component of the electric field is an odd function in time. Eq. 2.5 gives the Fourier transformation integrals.

$$E_x(\omega) = \sqrt{\frac{2}{\pi}} \frac{eZ}{4\pi\varepsilon_0 b^2} \int_0^\infty \frac{(\gamma v t/b)\sin(\omega t)}{\left((\gamma v t/b)^2 + 1 \right)^{3/2}} dt \qquad E_y(\omega) = \sqrt{\frac{2}{\pi}} \frac{\gamma e Z}{4\pi\varepsilon_0 b^2} \int_0^\infty \frac{\cos(\omega t)}{\left((\gamma v t/b)^2 + 1 \right)^{3/2}} dt$$
$$B_z(\omega) = \frac{\beta E_y(\omega)}{c} \tag{2.5}$$

With the appropriate substitutions, tables provide solutions to the integrals of Eq. 2.5 as seen in

Ref. [4].

$$u = \frac{\gamma v t}{b} \qquad du\left(\frac{b}{\gamma v}\right) = dt \qquad \omega' = \frac{\omega b}{\gamma v}$$
$$\int_0^\infty \frac{u \sin(\omega' u)}{(u^2+1)^{3/2}} du = \omega' K_0(\omega') \qquad \int_0^\infty \frac{\cos(\omega' u)}{(u^2+1)^{3/2}} = \omega' K_1(\omega') \tag{2.6}$$

The Fourier transformation replaces the time variable with a frequency variable in the field equations. The frequency relates to photon energy by the Einstein's photon energy equation, $E = \hbar\omega$. The substitution of time with frequency allows for a flux of photons to replace the classical electromagnetic field.

The γ dependence of the field components is different because of the different t dependence of Eq. 2.6. The integrals in Eq. 2.6 shift the γ dependence of the field component equations. Eq. 2.7 gives the result of the integrals:

$$E_x(\omega) = \sqrt{\frac{2}{\pi}} \frac{eZ}{4\pi\varepsilon_0 b^2} \frac{b}{\gamma v} \frac{\omega b}{\gamma v} K_0\left(\frac{\omega b}{\gamma v}\right) \qquad E_y(\omega) = \sqrt{\frac{2}{\pi}} \frac{\gamma e Z}{4\pi\varepsilon_0 b^2} \frac{b}{\gamma v} \frac{\omega b}{\gamma v} K_1\left(\frac{\omega b}{\gamma v}\right) \tag{2.7}$$

γ is subsumed into the substitution from t to ω in the numerator of the x-component and becomes a part of the zeroth-order modified Bessel function upon integration. The y-component does not have a factor of t in the numerator, therefore the factor of γ remains outside of the integral, and it does not get subsumed into the first-order modified Bessel function. In Eq. 2.7, E_y carries an additional factor of γ in the numerator relative to the E_x. E_y is γ times larger then E_x.

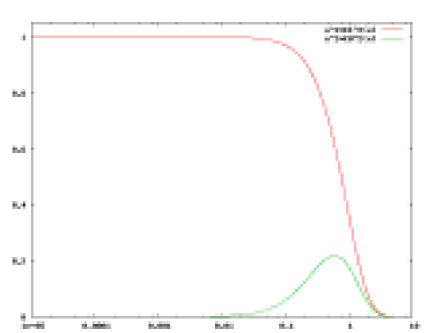

Figure 2.2: The zero and first order modified Bessel functions.

In the ultra-relativistic limit, the electric and magnetic fields have the same configuration as electromagnetic plane wave radiation. The electric and magnetic fields are perpendicular and related by a factor of c in the ultra rel-

ativistic limit. When v approaches c, $\beta \approx 1$,
the y-component of the electric field and the z-component of the magnetic field are related by a factor of c, $E_y/c = B_z$. Because $K_0(x)$ is smaller than $K_1(x)$ for all x, when $\gamma >> 1$, E_y is approximately equally to $\gamma\, E_x$. The conditions imposed by the ultra-relativistic limit result in the relationship of Eq. 2.8.

$$\gamma >> 1 \rightarrow \gamma E_x >> E_x \rightarrow E_y >> E_x \tag{2.8}$$

The x-component of the electric field can therefore be ignored and the magnetic and electric fields are left perpendicular to each other. The six field components reduced to one electric component and one perpendicular magnetic field component, which have a configuration identical to a plane wave.

As with plane waves, the energy per area per time transfered by the electromagnetic field is given by the Poynting vector. The Poynting vector takes the simple form of a plane pulse propagating in the x direction.

$$\vec{\mathbf{S}} \equiv \vec{\mathbf{E}} \times \vec{\mathbf{B}}/\mu_0 = \left(E_y^2/c\mu_0\right)\hat{\mathbf{x}} = c\varepsilon_0 E_y^2 \hat{\mathbf{x}} \tag{2.9}$$

The Poynting vector relates to the fluence (energy per unit area) [5],

$$I(b) = \hat{\mathbf{x}} \cdot \int_0^\infty \vec{\mathbf{S}} d\omega = \int_0^\infty \left(c\varepsilon_0 E_y^2\right) d\omega = \int_0^\infty \left(\frac{dI}{d\omega}\right) d\omega \tag{2.10}$$

and the spectral fluence (energy per area per frequency).

$$\frac{dI}{d\omega} = c\varepsilon_0 E_y^2 = \frac{e^2 Z^2 c}{4\pi^3 b^2 v^2 \varepsilon_0}\left(\frac{\omega b}{\gamma v}\right)^2 K_1^2\left(\frac{\omega b}{\gamma v}\right) = \alpha\hbar\left(\frac{Z}{b\beta\pi}\right)^2\left(\frac{\omega b}{\gamma v}\right)^2 K_1^2\left(\frac{\omega b}{\gamma v}\right) \tag{2.11}$$

Substituting Eq. 2.7 into Eq. 2.10 gives the Poynting vector as a function of frequency. Eq. 2.11 paves the way for Einstein's equation. The spectral fluence given by Eq. 2.11 relates the frequency to energy, which are the same quantities present in Einstein's equation.

Einstein's equation, $E = \hbar\omega$, gives the energy of a photon, which is related to the spectral fluence. If the fluence is due to a photon number density, N, Einstein's equation relates N to the fluence. The relationship between the number of photons per unit area in an infinitesimal energy range and the spectral fluence in an infinitesimal frequency range is given by Eq. 2.12 [3].

$$\frac{dI}{d\omega}d\omega = \hbar\omega N(\omega)d(\hbar\omega) \rightarrow \frac{1}{\hbar^2\omega}\frac{dI}{d\omega} = N(\omega) \tag{2.12}$$

Plugging Eq. 2.11 into Eq. 2.12 yields the semiclassical photon flux of an ultra-relativistic nucleus.

$$N(\omega,b) = \frac{\alpha}{\hbar\omega}\left(\frac{Z}{b\beta\pi}\right)^2\left(\frac{\omega b}{\gamma v}\right)^2 K_1^2\left(\frac{\omega b}{\gamma v}\right) \tag{2.13}$$

Eq. 2.13 replaces the classical electric field of a point charge with a semiclassical field of photons. Physicists can calculate the electromagnetic interactions between nuclei with the final result of the Weizsäcker-Williams approximation, Eq. 2.13. The photon flux in Eq. 2.13 provides the electromagnetic input to the J/ψ photoproduction cross section calculation.

2.5 Vector Meson Dominance

The Vector Messon Dominace method for calculating the J/ψ photoproduction cross section has three main components. VMD approach is constructed from the Weizsiäcker-Williams photon flux, the VMD fit to the proton-electron data, and the Glauber model for calculating the nuclear cross sections from the proton-electron cross sections. The Weizsiäcker-Williams photon flux provides the probe. The proton-electron scattering data combine with the Glauber model create a picture of the initial state of the nucleus. Each of the different approaches to calculating the UPC J/ψ photoproduction cross section use these same elements. However, the different models each use the last two elements differently to produce different pictures of the nucleus and different cross sections values.

The photon flux in the photoproduction cross section calculation must be finite in order for the cross section to be meaningful. The Weizsiäcker-Williams approximation, Eq. 2.13, produces a divergence at $b = 0$. The probability of the nuclei interacting would exceed one if the photon flux were infinite. The divergence that arises at $b = 0$ from K_1 results in an unphysically infinite photon flux. Removing the divergence is necessary. Special treatment of impact parameter, b, where the colliding nuclei overlap eliminates the divergence.

A modulation of the photon flux can subdue the divergence at $b = 0$. A convolution of the photon flux with the nucleon number density functions of the colliding nuclei produces the necessary modulation. Eq. 2.14 gives the nucleon density of a single nucleus,

$$\rho_A(s) = \frac{\rho_0}{1 + exp[(s - R_{WS})/d)]} \tag{2.14}$$

In Eq. 2.14, s is the distance from the center of the nucleus, R_{WS} is the radius of the nucleus, and d is the skin depth, which determines how quickly the nucleon density falls off beyond the nuclear radius. In Eq. 2.15 the depth of the nucleus is integrated out leaving just the transverse dimension in T_A. The average number of nucleons in the overlap region is given by a convolution of T_A from each of the two nuclei to produce T_{AA}.

$$\begin{aligned} T_A(\vec{r}) &= \int dz \rho_A(\sqrt{|\vec{r}|^2 + z^2}) \\ T_{AA}(|\vec{b}|) &= \int d^2\vec{r}\, T_A(\vec{r}) T_A(\vec{r} - \vec{b}) \end{aligned} \tag{2.15}$$

T_{AA} is the function that modulates the photon flux. As input to the Poisson distribution, T_{AA} reduces Eq. 2.13 at values of b where the nuclei overlap significantly and eliminates the divergence in the photon flux.

Modulating the photon flux by the probability that no nucleon-nucleon collisions occur limits the photon flux at low b in Eq. 2.13. The convolution of the photon flux with the b dependent probability that no nucleon-nucleon collisions occur removes the divergence in Eq. 2.13. Using the mean number of nucleons in the overlap region given by T_{AA}, the Poisson distribution gives the probability that no collisions occur at a given b:

$$P_0(b) = exp[-T_{AA}(b)\sigma_{NN}] \tag{2.16}$$

In Eq. 2.16, σ_{NN} is the cross section for a nucleon-nucleon interaction, which gives the probability that a collision will occur given the average number of nucleons in the overlap region. The average photon flux over impact parameter, b, can be calculated from the integration of the b-dependent photon flux, Eq. 2.13, with the b-dependent probability of having no nucleon-nucleon interactions, Eq. 2.16.

$$\frac{dN_\gamma(k)}{dk} = \int_0^\infty 2\pi b db P_0(b) \int_0^R \frac{rdr}{\pi R_A^2} \int_0^{2\pi} d\phi \frac{d^3N_\gamma(k, b + r\cos(\phi))}{dkd^2r} \tag{2.17}$$

Eq. 2.17 goes down to $b = 0$ where the photon flux is infinite, but because the probability of having a nucleon-nucleon collisions is high, the divergence is eliminated. The result of Eq. 2.17 does not diverge.

A power-law fit to the proton photoproduction data gives an analytic expression for the energy dependence of the proton photoproduction cross section. The fitting function is simple and only depends on the photon-proton center of mass energy, W. Eq. 2.18 gives the parameterization of the forward proton photoproduction cross section fit.

$$\left.\frac{d\sigma(\gamma p \to Vp)}{dt}\right|_{t=0} = b_v(XW^\varepsilon + YW^{-\eta}) \tag{2.18}$$

W is the center of mass energy of the proton-photon system in Eq. 2.18. The remaining variables in Eq. 2.18 are simple power-law fit parameters. The XW^ε term characterizes pomeron mediated interactions, and the YW^η term characterizes meson mediated interactions[6]. J/ψ's high mass relative to the π and ρ renders the second term in Eq. 2.18 negligible as the term falls rapidly with increasing W. Eq. 2.18 allows for extrapolation and interpolation of the measured forward proton photoproduction cross section. The fit to the data provides estimates for energies that have not yet been probed experimentally.

The proton-electron scattering data is used differently in the VMD method than in the other major methods. The VMD method for calculating UPC photoproduction cross sections relies more on electron-proton scattering data. The proton photoproduction cross sections from the electron-proton scattering data is a direct input to the VMD model. A power-law fit to the proton photoproduction data, as opposed to model dependent gluon densities of other approaches, combines with the Glauber model to provide the nuclear model in the VMD method. Because of the simplicity of the method, the VMD approach incorporates less modifications of the nuclear initial state relative to the proton initial state. As a result, the VMD method produces a higher UPC J/ψ photoproduction cross section relative to the other methods.

Vector meson dominance and the optical theorem allow for the calculation of the total proton-meson scattering cross section from the fit given by Eq. 2.18. The optical theorem relates a total cross section, σ, to a corresponding forward scattering cross section, $d\sigma/dt|_{t=0}$. Vector meson dominance asserts that the colored part of the photon wave function is dominated by vector mesons; therefore, the photon is represented as a quark-antiquark pair in photoproduction calculations. These two components combine to produce Eq. 2.19.

$$\begin{aligned} \frac{d\sigma(\gamma p \to Vp)}{dt}\Big|_{t=0} &= \frac{4\pi\alpha}{f_v^2(M_V,\Gamma_{l^+l^-})}\frac{d\sigma(Vp \to Vp)}{dt}\Big|_{t=0} \\ \sigma(Vp)^2_{tot} &= 16\pi\frac{d\sigma(Vp \to Vp)}{dt}\Big|_{t=0} \end{aligned} \tag{2.19}$$

In Eq. 2.19, the photon-proton scattering is related to meson-proton scattering through the photon-meson coupling, which depends on the vector meson's mass, M_V, and leptonic decay width, $\Gamma_{l^+l^-}$. The result of combining vector meson dominance and the optical theorem in Eq.2.19 provides the cross section for a meson to scatter off a proton. The total proton-meson scattering cross section, provides the input to the Glauber model calculation of the nuclear photoproduction cross section.

The nucleus-meson scattering cross section relates to Eq. 2.19 through the Glauber model. The Glauber model allows for Eq. 2.19, the proton-meson scattering cross section, to be used to calculate a nucleus-meson scattering cross section. The Glauber model produces nuclear cross section calculations from nucleon (proton or neutron) interaction cross sections by use of T_{AA}. The combination of the mean number of nucleons in the overlapping region of a nucleus-nucleus collision, T_{AA}, the nucleon cross section, σ, and the Poisson distribution make-up the core of the Glauber model. For the total nucleus-meson scattering cross section, the equation has the following form:

$$\sigma_{tot}(VA) = \int d^2\vec{r}(1 - e^{-\sigma_{tot}(Vp)T_{AA}(\vec{r})}) \tag{2.20}$$

In Eq. 2.20, the term $e^{\sigma_{tot}(Vp)T_{AA}}$ gives the probability of having no meson-nucleon scatterings from the Poisson distribution. The probability of having at least one scattering is given by subtracting one from the term $e^{\sigma_{tot}(Vp)T_{AA}}$ in Eq. 2.20. As seen in Eq. 2.20, the Glabuer model leverages scientific knowledge of the proton to understand of the nucleus. The Glauber model is the tool that combines the proton photoproduction data with nucleon distributions in the nucleus to produce a nuclear vector meson photoproduction cross section in the VMD approach.

Reversing the process used for the proton, Eq. 2.20, the meson nucleus scattering cross section, relates to forward nuclear photoproduction cross section through the optical theorem. The nuclear photoproduction cross section is the input to the calculation of the final result, the nuclear vector meson photoproduction cross section in UPC events. Eq. 2.21 uses the optical theorem to produce the nuclear photoproduction cross section from the nucleus-meson scattering cross section:

$$\begin{aligned} \frac{d\sigma(\gamma A \rightarrow VA)}{dt}\Big|_{t=0} &= \frac{\alpha\sigma_{tot}^2(VA)}{4\pi f_v^2} \\ \sigma(\gamma A \rightarrow VA) = \frac{d\sigma(\gamma A \rightarrow VA)}{dt}\Big|_{t=0} &\int_{t_{min}}^{\infty} dt|F(t)|^2 \end{aligned} \tag{2.21}$$

F in equation Eq. 2.21 is the Fourier transform of the nuclear density function, ρ_A. To produce the formula for calculating the UPC vector meson photoproduction cross section, Eq. 2.21 is combined with the photon flux incident on the nucleus, Eq. 2.17.

$$\sigma(AA \rightarrow AAV) = 2\int dk \frac{dN_\gamma}{dk}\sigma(\gamma A \rightarrow VA) \tag{2.22}$$

The factor of 2 in Eq. 2.22 comes from the fact that both of the two colliding nuclei contribute. Combining the three elements of VMD, Eq. 2.22 is the final result of the VMD UPC photoproduction cross section calculation. Vector meson production rates in UPC collisions are predicted by Eq. 2.22, which can be confirmed or denied by experiment.

2.6 Leading Twist Approach Derivation

The LTA method for calculating UPC photoproduction cross sections combines elements of the Glauber model with direct use of gluon densities. The proton gluon density is modified by a nuclear modification function in the LTA method to produce the nuclear gluon density. The nuclear modification function converts the proton photoproduction cross section to a nuclear photoproduction cross section in the LTA method. The LTA method is different from the other methods in its direct use of the nuclear modification factor and how the nuclear modification factor calculation incorporates multiple scattering. The direct use of the nuclear modification factor produces the most gluon shadowing out of the three major methods, and results in the lowest cross sections. The LTA method is the easiest to constrain experimentally for this reason.

The LTA method uses the Weizsiäcker-Williams approximation to calculate the photon flux created by the colliding nuclei. As in the VMD method, the probability of having no hadronic collisions modulates the flux. The photon flux for the LTA method has the following form [7]:

$$n^i_{\gamma/A}(\omega_\gamma) = \frac{2\alpha Z^2}{\pi}\int_{b_{min}}^{\infty} db \frac{x^2}{b}\left[K_1^2(x) + \frac{K_0^2(x)}{\gamma_L^2}\right] P_0(b) P_C^i(b) \qquad (2.23)$$

$$x = \frac{\omega b}{\gamma_L v}$$

The $K_0^2(x)$ term contributes a photon flux in the transverse direction. $P_C^i(b)$ is an additional modulation factor that requires various additional interactions. These interactions result in additional emissions of neutrons from the receding nuclei as the nuclei relax from excited states. The LTA flux reproduces the VMD result when the K_0 term becomes negligible as γ_L approaches ∞ and

$P_C^i = 1$ when all emissions are allowed. The terms P_C^i and K_0 create additional ways to distinguish UPC events from nuclear collisions experimentally but leave the underlying interaction mechanism the same. For example, the additional terms in the LTA formulation of the photon flux produce calculations of asymmetric neutron emission, which separate UPC events from nuclear collisions.

The LTA method calculates the nucleon photoproduction cross section from the nucleon gluon density. Ref. [7] derives the nucleon cross section from derivations of the nucleon gluon densities from electron-proton scattering data and leading order perturbative quantum field theory calculations. The forward photoproduction cross section of the nucleon has the following form [7]:

$$\frac{d\sigma_{\gamma N \to J/\psi N}(t=0)}{dt} = \frac{16\Gamma_{l^+l^-}\pi^3}{3\alpha M_{J/\psi}^5}[\alpha_s \mu^2 x G_N(x,\mu^2)]^2 \tag{2.24}$$

Here G_N is the gluon density of the nucleon, x is the fraction of the nucleon's momentum the gluon carries, and μ is related to momentum at which the nucleon is being probed, which is equal to $M_{J/\psi}/2$ for J/ψ photoproduction. In Eq. 2.24 the nucleon cross section is explicitly connected to the gluon density. By connecting the gluon density to the cross section, Eq. 2.24 allows for the gluon density to be experimentally probed.

Ref. [7] exploits the optical theorem to relate the forward photoproduction cross section of the nucleon to the nuclear cross section. Eq. 2.25 gives the relation:

$$\sigma_{\gamma A \to J/\psi A}(\omega) = \frac{d\sigma_{\gamma N \to J/\psi N}}{dt}(\omega, t_{min}) R_g^2 \int_{t_{min}}^{\infty} dt |F(t)|^2 \tag{2.25}$$
$$R_g = \frac{G_A(x,\mu^2)}{AG_N(x,\mu^2)}$$

R_g, the nuclear modification function, is the ratio between the gluon density of the nucleon, G_N, to the gluon density of the nucleus, G_A. As with the VMD method, the optical theorem relates the forward cross section, $\frac{d\sigma_{\gamma N \to J/\psi N}}{dt}(\omega, t_{min})$, to the total cross section, $\sigma_{\gamma A \to J/\psi A}$. The LTA method relates the measurable UPC photoproduction cross section to the gluon density of the nucleus. Eq. 2.25 further connects the gluon density of the nucleon to the relative reduction of the gluon density in the nucleus through R_g.

From Eq. 2.25, the LTA method can predict the angular distribution of photoproduced J/ψ with respect to the beam axis. In Ref. [8] the angular distribution is expressed in the form of the rapidity dependency of the UPC photoproduction cross section.

$$\frac{d\sigma_{A_1A_2\to A_1A_2J/\psi}}{dy} = n_{\gamma/A_1}(y)\sigma_{\gamma A_2\to J/\psi A_2}(y) + n_{\gamma/A_2}(-y)\sigma_{\gamma A_1\to J/\psi A_1}(-y) \tag{2.26}$$
$$y = ln\left(\frac{2\omega}{M_{J/\psi}}\right)$$

Eq. 2.26 is comprised of two terms, one for photons from the forward going nucleus interacting with the backward going nucleus, and a second for the reverse situation. The integration of Eq. 2.26 over y produces the factor of 2 that is present in Eq. 2.22. The rapidity distribution of the photoproduction cross section given in Eq. 2.26 provides a more detailed prediction and allows for more direct experimental comparison. Eq. 2.26 allows for comparison to rapidity regions that are covered by experiments.

The LTA method is distinct from the pQCD method and VMD method through the use R_g, the nuclear gluon modification factor. As opposed to using R_g, the pQCD method uses the nuclear gluon density, and VMD model uses proton photoproduction cross sections directly. In the LTA method, R_g is calculated through a combination of J/ψ photoproduction data from proton-electron scattering and DGLAP evolution equations, which incorporates nuclear multiple scattering effects [7]. The DGLAP evolution equations give the depends of nuclear gluon densities on the momentum scale at which the nucleus is probed, μ in Eq. 2.24. The unique way the LTA method calculates R_g results in lower cross sections than the other major methods and allows for experimental sensitivity. Experimental measurements of the UPC J/ψ photoprodcution cross section with CMS have the opportunity to distinguish whether R_g as calculated in the LTA method accurately predicts the gluon density of the nucleus.

2.7 Perturbative Quantum Chromo-dynamics

To calculate the UPC J/ψ photoproduction cross section, the pQCD method uses the nuclear gluon density to characterize the nucleus and the Weizsäcker-Williams approximation for the probing photon flux. The pQCD method combines these components such that the nuclear gluon density is a direct variable. The nuclear gluon density term in the pQCD formulation allows for the use of a variety of nuclear gluon density models. A range of nuclear gluon densities are present in the available models resulting in a wide range of cross section values. The UPC J/ψ photoproduction cross section is correlated with the gluon density of the nucleus rising with higher densities and shrinking with lower densities. In the pQCD approach, the calculation of the UPC J/ψ photoproduction cross section allows experiments to constrain many different nuclear gluon density models.

In the pQCD method, the photon interacts with the nucleus by fluctuating to a quark-anitquark pair. For J/ψ, the photon fluctuates to a $c\bar{c}$ pair. The probability for the photon to fluctuate to a $c\bar{c}$ pair depends on the $M_{J/\psi}$, the mass of J/ψ, $\Gamma_{l^+l^-}$, the J/ψ leptonic decay width, and α, the electromagnetic coupling constant. These three variables connect the c quark to the electromagnetic force mediator, the photon. Recast as a $c\bar{c}$ pair, the photon couples to the nuclear gluon density. Ref. [9] uses the fluctuation of the photon to a $c\bar{c}$ pair as the foundation for calculating the forward J/ψ photoproduction cross section.

The $c\bar{c}$ pair arising from the photon fluctuation scatters off the gluons of the nucleus. The density of gluons in the nucleus determines how likely and therefore how large the cross section is for the quarks to scatter and form a J/ψ. The forward scattering cross section is the portion of those scattering events which transfer the minimum amount of momentum between the photon and the nucleus. The forward cross section for J/ψ photoproduction in the nucleus has the following form [9]:

$$\frac{d\sigma_{\gamma A\rightarrow J/\psi A}}{dt}\Big|_{t=0} = \xi_{J/\psi}\Big(\frac{16\pi^3\alpha_s^2\Gamma_{l^+l^-}}{3\alpha M_{J/\psi}^5}\Big)[xG_A(x,\mu^2)]^2 \tag{2.27}$$

In Eq. 2.27, $\xi_{J/\psi}$ is an experimentally derived correction factor, α_s is the strong coupling constant,

x is the momentum faction of the nucleus the scattering gluons carry, and G_A is the gluon density of the nucleus. Both the c and $\bar{c}$ couple to the gluon density, and the double coupling results in the squared dependence of the cross section on the gluon density in Eq. 2.27. Fitting Eq. 2.27 to proton-electron scattering data sets $\xi_{J/\psi}$ [9]. The forward scattering cross section given by Eq. 2.27 connects the photon flux to the gluon density and provides the input to calculate the total cross section by the optical theorem. Eq. 2.27 is the crux of how UPC measurements provide insight into the gluon content of the nucleus.

The optical theorem relates the forward cross section in Eq. 2.27 to the total photoproduction cross section. The total cross section calculated by use of the optical theorem gives the probability that a photon incident on the nucleus will produce a J/ψ regardless of the momentum transfered in the interaction. Ref. [9] gives the form of the total cross section equation:

$$\sigma_{\gamma A\to J/\psi A}(k) = \frac{d\sigma_{\gamma A\to J/\psi A}}{dt}\Big|_{t=0} \int_{t_{min}(k)}^{\infty} dt |F(t)|^2 \tag{2.28}$$

Here $t_{min} = (M_{J/\psi}^2/4k\gamma_L)^2$, which is the minimum amount of momentum transfer required to produce a J/ψ given the photon wave number k. The k dependence of t_{min} produces the rapidity, y, dependence of the total cross section. The total cross section for photoproduction, Eq. 2.28, provides the input to Eq. 2.26, which gives the rapidity dependence of the UPC photoproduction cross section. Eq. 2.28 as input to Eq. 2.26 allows for experimental comparison of the pQCD method to measurements of UPC photoproduction cross sections. With the pQCD method's direct use of the nuclear gluon density in Eq. 2.27, the pQCD method allows for experimental exploration of any gluon density model.

2.8 Incoherent Photoproduction

2.9 Photon Induced Nuclear Break-up

2.10 Theoretical Results

The UPC photoproduction cross section calculations depend significantly on how the nucleus is represented in the calculation. The results from the VMD, LTA, and pQCD methods vary from a relatively large cross section in the VMD model, ranging through a variety of values in the pQCD method, to a relatively small cross section in the LTA method. Each of these methods utilizes the same probe of the nucleus, the equivalent photon flux that is calculated using the Weizsiäcker-Williams approximation. The three methods deviate in how they calculate the forward photoproduction scattering cross section. The differences in the UPC photoproduction cross sections predicted by the different models demonstrates the amount of experimental sensitivity there is to distinguishing between the models. The dependence of the cross section on rapidity shows where in phase space a measurement of the cross section is most sensitive.

The predicted value for the UPC J/ψ photoproduction cross section in PbPb collisions at the LHC differ widely depending on which of the three main methods is used. The cross section value calculated by Eq. 2.22 in the VMD, LTA, and the various gluon density models in pQCD method vary significantly. Table 2.1 gives the predicted values for the three main methods taken from Ref [10], Ref [7], and Ref [6]. The cross sections in Table 2.1 differ by a factor of ≈ 4 from the smallest to largest and create an experimental opportunity. The clear discrepancy between the models in Table 2.1 demonstrates the high amount of experimental sensitivity there is for distinguishing between the models.

The rapidity dependence of the cross sections determine which values of rapidity will be most sensitive to differences in the models. The rapidity dependence calculated by Eq. 2.26 overlap between the models at certain values of y leaving the models indistinguishable at that rapidity. Fig. 2.3 [11] shows the rapidity dependency of the UPC J/ψ photoproduction cross section for the

Model	$\sigma_{AA\rightarrow AAJ/\psi}(mb)$
VMD/STARlight MC	23
LTA	9
pQCD-MSTW08	34
pQCD-EPS08	7
pQCD-EPS09	14
pQCD-HKN07	23

Table 2.1: $\sigma_{AA\rightarrow AAJ/\psi}(mb)$ the LTA, VMD, pQCD methods. Four different gluon density models are used in the pQCD method. STARlight is a simulation software package that utilizes the VMD model.

three main models including several different gluon density models using the pQCD method. In

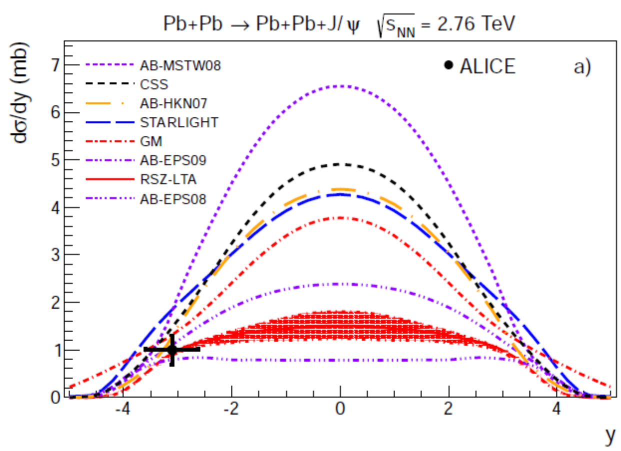

Figure 2.3: AB is the pQCD method, RSZ-LTA is the LTA method, and STARlight is the VMD model.

Fig. 2.3 at higher rapidities, in particular $|y| > 3$, the various models give similar values for $d\sigma/dy$. At $y = 0$ the models vary the most. Fig. 2.3 shows that experiments that can measure J/ψ at $y = 0$ have the best opportunity to distinguish between the models. The high sensitivity at $y = 0$ creates an advantage for experiments that can measure particles with small rapidity and low momentum.

The UPC photoproduction models each have different shapes to their rapidity dependence. The slope of $d\sigma/dy$ in Fig. 2.3 depends on the model. Through the rapidity region $1 < |y| < 3$, each of the models has a progressively steeper slope. The LTA method and the pQCD method utilizing the EPS08 gluon density model are relatively flat where as the VMD and other gluon density models using the pQCD method have a noticeable slope. The differing slopes provide an additional experimental observable. The shape of the rapidity distributions provide experimental sensitivity at rapidities away from $y = 0$ and creates an opportunity for experiments that can not measure J/ψ at $y = 0$.

The nuclear suppression factor, S, demonstrates the difference between how the models represent the nucleus. S, which is a ratio between the nuclear photoproduction cross section and the free nucleon photoproduction cross seciton, is a measure of how the nuclear gluon densities evolve in each of the models. Fig. 2.4 from Ref.[12] shows the nuclear suppression, which is equivalent to R_g in Eq. 2.25, for the LTA and pQCD method. Fig. 2.5 shows the nuclear suppression for

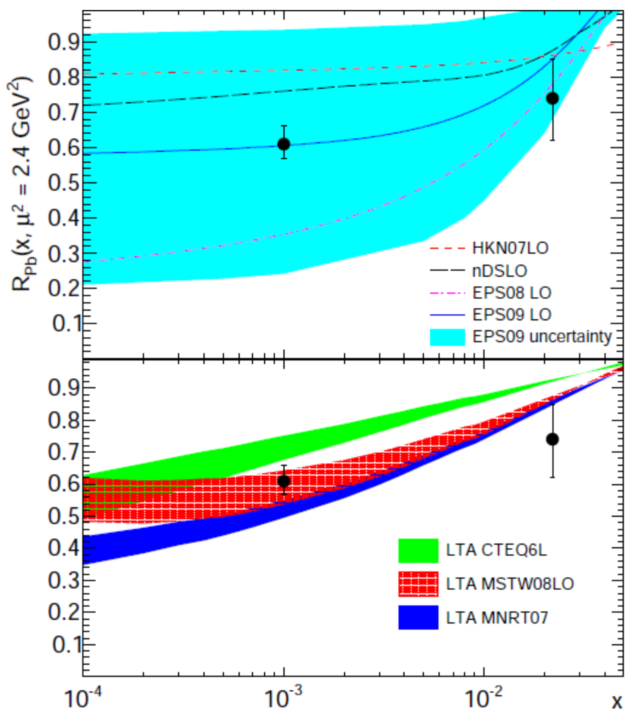

Figure 2.4: Nuclear supression factor, S, in the pQCD and LTA methods.

the VMD method [12]. Fig. 2.5 and Fig. 2.4 show that as the momentum of the probing photon goes up, increasing $W_{\gamma p}$, and momentum of the probed gluon goes down, decreasing x, the nuclear gluon density decreases relative to the free nucleon. The nuclear suppression factor, S, allows for the different models' representations of the gluon content of the nucleus to be directly compared to each other and to data. S can be measured from data by assuming a Weizsiäcker-Williams photon

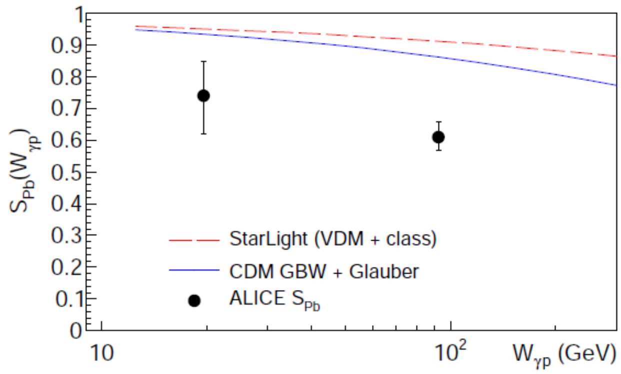

Figure 2.5: Nuclear supression factor, *S*, in VMD method.

flux and provides insight into nuclear gluon densities.

Chapter 3

The CMS Detector

CMS is housed at interaction point 5 of the LHC. The LHC is designed to pursue physics at the TeV scale. This is the scale where electroweak symmetry breaking is believed to occur [**?**]. While this means that the search for the standard model Higs is the central driving design consideration, the wide range of possibilities for finding new physics signals requires a general purpose detector. The expedient discovery of new physics through low cross section interactions requires high luminosity. This consideration leads inevitably to pile up, where multiple collisions occurs at a single bunch crossing. At peak luminosity the LHC is expected to produce on average 20 hard proton-proton (pp) collisions per bunch crossing [1]. These particle physics considerations of high multiplicity due to pileup and the need for a general purpose detector make CMS serendipitously well suited for heavy ion physics.

The general purpose design of CMS is dominated by the massive 4T superconducting solenoid at its core. The magnets is 13m long with a 6m diameter, and pushes the limits of power and compactness [1]. These two conflicting limits are achieved through the novel design of interweaving structural and conducting elements together in the coil of the solenoid.

Within the solenoid resides three different sub detectors. The inner most is the world's largest silicon tracker [1]. The tracker is surrounded by a highly effective lead tungstate crystal electromagnetic calorimeter (ECAL). ECAL is encapsulated in a brass scintillating hadronic calorimeter

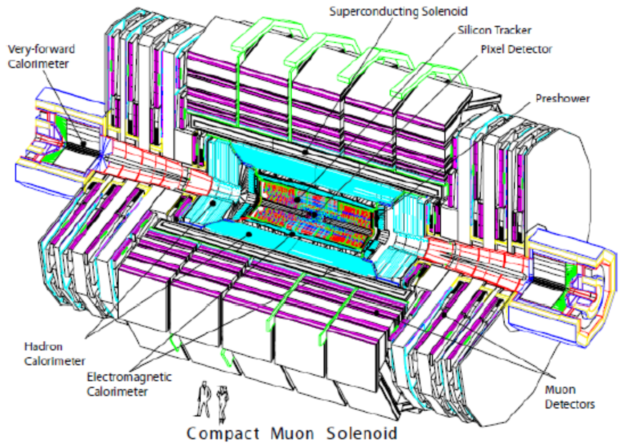

Figure 3.1: The Compact Muon Solenoid from Reference [1].

(HCAL). Outside the magnet, muon chambers are used to aid in the measurement and triggering of muon events. Altogether CMS weighs 12,500 metric tons, has a diameter of 14.6m, and a length of 21.6m [1].

The Silicon Tracker is the innermost sub-detector of CMS, and has active elements as close as 4.4cm to the interaction point [1]. The tracker has a length 5.8m, a diameter of 2.6m and covers a range in pseudorapidity of $|\eta| < 2.5$. Pseudorapidity is defined as $\eta \equiv -\ln(\tan(\theta/2))$, where θ is the polar angle, and ϕ is the azimuthal angle with respect to the beam axis. At the center of the tracker are three rings of silicon pixels around the beam with two disks of silicon pixels to cap the rings. The pixel portion of the silicon tracker is comprised of $66\text{x}10^6$ pixels. The silicon pixels are surrounded by silicon strips. The silicon strips are separated into 4 different sections: the Tracker Inner Barrel, the Tracker Inner Disk, the Tracker Outer Barrel, and the Tracker End Caps. The silicon strip detectors as a whole are comprised of $9.3\text{x}10^6$ silicon strips. The high number of pixels and strips allow for the ability to distinguish and collect enough distinct points to reconstruct the path of the 1000 or so charge particles per bunch crossing expected at peak luminosity [1].

The next detector beyond the tracker is ECAL. ECAL is made of 61,200 lead tungstate ($PbWO_4$) crystals in the central barrel and 7,324 on each of the two endcaps [1]. The barrel (EB) covers a pseudorapidity range $|\eta| < 1.479$ and has an approximate $\eta - \phi$ segmentation of 0.0174×0.0174. Lead tungstate is very dense, which is reflect in the high number of interaction lengths the short depth of one crystal provides. The crystals of the barrel have a depth of 230 mm corresponding to 25.8 radiation lengths (X_0). The radiation length is the mean distance a high energy particle travels before giving up one e-fold of kinetic energy through electromagnetic interactions. For example, after one radiation length $E \to E/e$, where $e = 2.71828183$. The endcaps (EE) cover the psuedo-rapitity region $1.479 < |\eta| < 3$. In the endcap the crystals have an exposed area of 28.62×28.62 mm^2, and a depth of 220 mm corresponding to 24.7 X_0. The energy resolution of the ECAL as measured by test beam data can be seen in Figure 3.2.

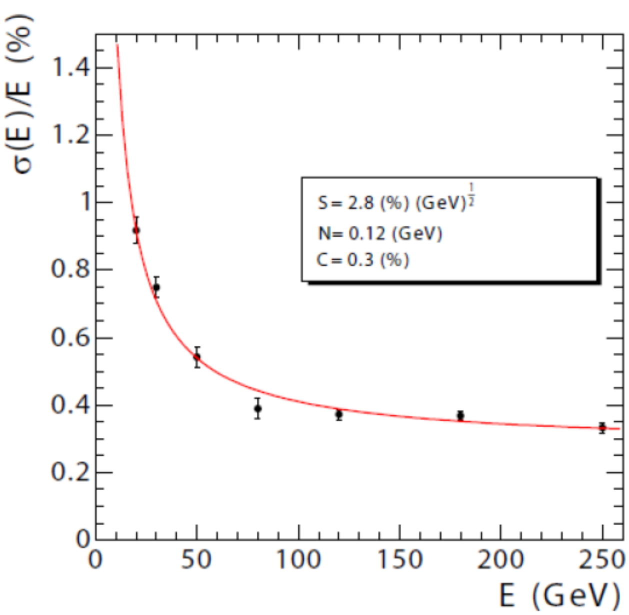

Figure 3.2: The energy resolution of ECAL as a function of energy from Reference [1].

The HCAL like the ECAL has both a barrel (HB) and endcaps (HE). The pseudorapidity region $|\eta| < 1.3$ is covered by HB [1]. HB has an $\eta - \phi$ segmentation of 0.0897×0.0897, and is 25 times more sparsely granulated than EB. HE covers the pseudorapidity region $1.3 < |\eta| < 3$. HE, like EE and the tracker endcaps, is aligned perpendicular to the beam axis resulting in granularity that changes with η. In the region $1.3 < |\eta| < 1.6$ HE has an $\eta - \phi$ segmentation of 0.0897×0.0897. The $\eta - \phi$ segmentation roughly doubles to 0.17×0.17 in the region $1.6 < |\eta| < 3$. The energy resolution of the barrel and endcaps can be seen in Figure 3.3. The thickness of the hadronic calorimeter is best described in interaction lengths, the mean distance for a particle to give up an e-fold of energy through nuclear interactions. At $\eta = 0$ the barrel has a thickness 5.82 interaction lengths (λ_I), and increases as the path length through the material increases to 10.6 λ_I at $|\eta| = 1.3$.

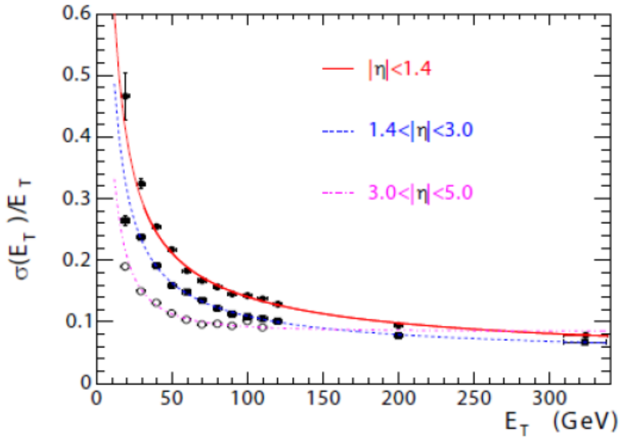

Figure 3.3: The E_T resolution of HCAL as a function of $|\eta|$ and E_T from Reference [1].

In addition to HB and HE, HCAL has two additional calorimeters. Because the space between ECAL and the magnet is restricted to 1.18 m, an outer hadronic calorimeter section (HO) is placed beyond the magnet in the region $|\eta| < 1.3$ [1]. The main function of HO is to collect energy from the highest energy hadrons before they reach the muon system. HO is not used in this analysis, but does contribute to the material budget. To increase the total calorimetric coverage, HCAL also has a quartz fiber calorimeter (HF) in the forward region, $3 < |\eta| < 5$. For the majority of HF's 13 η rings the $\eta - \phi$ segmentation is 0.175×0.175. In the lowest $|\eta|$ ring the segmentation is 0.111×0.175 in $\eta - \phi$. In the highest two $|\eta|$ rings the segmentation in ϕ is 0.349, with an η segmentation of 0.175 in the outer and 0.300 in the innermost ring. The longitudinal direction is effectively segmented by using short fibers and long fibers. The measure energy deposited deeper than 22 cm is measured in both the short and long fibers, where as the long fibers are present throughout. This allows electromagnetic showers to be distinguished from purely hadronic showers [1]. The energy resolution for HF can be seen in Figure 3.3.

Beyond HF there are two more detectors in the forward region. CASTOR covers the range 5.2 $< \eta <$ 6.6 on the positive side of the beam. The Zero Degree Calorimeters (ZDC) sit between the beam pipes on either side of the interaction point covering the area around $\theta = 0$, $|\eta| > 8.3$. Both detectors are tungsten quartz Cerenkov detectors, and can contribute to the proposed measurement. In heavy ion collisions the ZDC has the ability to measure neutral particles that do not participate in the collision [1]. CASTOR extends the total coverage of the CMS as whole giving more access to low-x physics [1].

The muon system resides just outside of the superconducting magnet. It consists of three complementary systems: drift tube (DT) chambers in the barrel, cathode strip chambers (CSC) in the endcaps, and resistive plate chambers (RPC) in both the barrel and endcap regions [1]. Ultimately the muon system is most useful for triggering on muons [1].

The heavy ion community is making use of the capabilities of CMS in a myriad of ways. The muon trigger has been used in the search for suppression of quarkonium states. This is an important probe of the correlation length within the hot dense state known as the quark gluon plasma (QGP). The tracker has been utilized for to study charged particle multiplicities, and and elliptical flow, two probes of the thermal expansion of the QGP. HCAL has aided in measuring jet suppression, which probes the strength with which the QGP interacts with strong interacting objects. Through its general purpose design and its ability to handle the high multiplicities produce by the LHC, CMS proves to be an excellent detector for investigating strongly interacting mater through heavy ion collisions.

3.1 Trigger

The CMS trigger is two teired. The L1 trigger is the lower level hardward based system. The High Level Trigger (HLT) is software base and runs on a computer farm at point 5 where CMS is housed.

Chapter 4

Analysis

4.1 MC Simulation

Monte Carlo (MC) simulations are used to understand how the detector effects the measurement. Two main classes of Monte Carlo (MC) simulation samples were used. The first class uses STARlight to generate events. The Second class uses PYTHIA6 to create and decay J/ψs with a given input p_T and rapidity distribution.

4.2 Trigger Development

Prior to the 2011 LHC PbPb run, UPC events had not been directly studied in PbPb collisions using CMS. Design of the UPC triggers required studies of the 2010 data to estimate rates and insure that the bandwidth used by these trigger would be sufficiently low. All the different physics analyses must share the limited readout rate of the detector. For this reason, conservation of bandwidth was a major design consideration.

To estimate the 2011 rates prior to the run, the 2010 rates were used to extrapolate to the interaction rate of the 2011 run. The unique UPC triggers were estimated by combining existing triggers from the 2010 run. By calculating the ratio between the UPC trigger rates and the minimum bias trigger rate, the UPC trigger rates were scaled up to the 2011 interaction rates using the

2010 data. The extrapolated rates allowed for a package triggers to be created, which fit within the bandwidth requirement of CMS Heavy Ions.

The trigger package for 2011 contained ZDC based efficiency monitoring triggers, muon and electron based triggers for measuring J/ψ, and backup triggers in case there was a problem with the original muon and electron triggers. In order to recorded the trigger efficiency monitoring data, the ZDC triggers had to be prescaled to a lower rate. The scaling down of the monitoring triggers were setup to insure overlap with the signal triggers. By balancing the competing objectives of rate reduction and increasing the overlap between the monitoring and signal triggers, the prescales for the trigger were as seen in Table .

4.2.1 L1 Trigger

The goal of the L1 triggers was to record enough data to measure dimuons and dielectrons in UPC events. To achieve this, the loosest muon trigger and lowest threshold ECAL triggers where paired with a trigger on energy in the ZDC and a veto on energy in the BSC or HF. The L1 package that was constructed for the analysis of UPC J/ψ is presented in Table 4.1.

L1 Trigger Seed	Type
L1_MuOpen_ZdcCalo_NotBscMinBiasThresh2_BptxAND	Physics
L1_EG2_ZdcCalo_NotBscMinBiasThresh2_BptxAND	Physics
L1_EG5_ZdcCalo_NotBscMinBiasThresh2_BptxAND	Physics
L1_ZdcCaloMinus_BptxAND	Monitor
L1_ZdcCaloMinus_BptxAND	Monitor
L1_MuOpen_ZdcCalo_NotHcalHfCoincidencePm_BptxAND	Backup
L1_EG2_ZdcCalo_NotHcalHfCoincidencePm_BptxAND	Backup
L1_EG5_ZdcCalo_NotHcalHfCoincidencePm_BptxAND	Backup

Table 4.1: List of 2011 L1 seeds.

The cumulative L1 trigger rate for all the UPC L1 trigger seeds was required to be 200 Hz. This requirement stemmed from the need to keep the tracker read-out rate low. The trackers baseline voltage can fluctuate due to the high tracker hit multiplicities in PbPb collisions. In order to monitor the zero suppression of the tracker, the zero suppression algorithm was executed using the HLT computing farm rather than the in the tracker firmware. The additional computing cycles needed to run the zero suppression the limit for L1 bandwidth.

4.2.2 HLT Trigger

As opposed to the L1 trigger, which reads out the tracker, the HLT has access to the tracker information. Reconstruction of a track in the pixel detector is used by the UPC paths. The use of the pixel detector only, as opposed to using the whole tracker including the silicon strip detector, allows for quick track reconstruction saving computing cycles. The requirement of at least on reconstructed pixel track for the HLT triggers was designed to reject backgrounds where no particles are reconstructed by the tracker.

HLT Trigger	
HLT_HIUPCNeuMuPixel_SingleTrack	Physics
HLT_HIUPCNeuEG2Pixel_SingleTrack	Physics
HLT_HIUPCNeuEG5Pixel_SingleTrack	Physics
HLT_HIMinBiasZDC_Calo_PlusOrMinus_v1	Monitor
HLT_HIMinBiasZDC_PlusOrMinusPixel_SingleTrack_v1	Monitor
HLT_HIUPCNeuHcalHfMuPixel_SingleTrack	Backup
HLT_HIUPCNeuHcalHfEG2Pixel_SingleTrack	Backup
HLT_HIUPCNeuHcalHfEG5Pixel_SingleTrack	Backup

Table 4.2: List of 2011 HLT trigger.

The total HLT output for the UPC trigger paths was 20 Hz. The limiting factor for the HLT rate was the amount of disk space available to store the data.

4.3 Data Sets and Event Selection

4.3.1 Data Set

In order to investigate novel physics processes like UPC J/ψ production, the LHC has delivered unprecedented amounts of data. The data for this analysis was recorded during the 2011 LHC

PbPb run. During this period, 150 μb^{-1} where recorded by the CMS detector, corresponding to over a billion PbPb collisions. Of this, 143 μb^{-1} are used in this analysis.

Three specially selected samples were used for the present analysis (see Table 4.3). These samples were recorded using subsets of the triggers found in Section 4.2. The J/ψ events discussed in this thesis were obtained analyzing the sample labeled in Table 4.3 as physics. A minimum bias sample was recorded for the sake of estimating efficiencies. Last, a zero bias sample was recored for investigating the ZDC and the noise distributions of HF. By recording this hierarchy of samples, interesting events are selected with a much higher purity in the physics sample, while the zero bias and minimum bias samples allow for the investigation of the selection criteria.

To record the physics sample containing the J/ψ signal, a muon trigger was paired with a veto on energy in the BSC and a requirement that there be energy in at least one of two sides the ZDC. This trigger utilizes the unlikely chance of having overlapping noise in in the ZDC and muon detector. Because of the characteristically low momentum of UPC J/ψ as compared to J/ψ created by other physics process, the loosest muon trigger was used. The trigger rejects muon noise by requiring that a interaction took place that deposits energy in the ZDC. Contributions from hadronic interactions are reduced by the veto on the BSC. In this way the balance between reducing the rate and maximizing the efficiency was struck, allowing for the data to be recorded without producing high rates resulting in dead time for the detector.

In order to investigate the muon trigger and the other parts of the events selection, a minimum bias sample was recorded using the ZDC. For ZDC triggered sample, any event which had energy consistent with at least one neutron in either of the two sides of the ZDC was recorded. This process is much more common than the UPC J/ψ production. For this reason, the rates of this trigger are much higher than the physics trigger, and only a small sub set of these events are recorded. From this trigger the pixel track efficiency was estimated.

In addition to the minimum bias and physics sample, a zero bias sample was recorded to examine the ZDC trigger and the HF noise distributions. The zero bias trigger fired every time both beams passed through CMS. Only 4 events out of every million triggered were recorded for this

Sample	Events	L_{int}
Physics	300K	143.3 μb
Minimum Bias	100K	X
Zero Bias	5M	580 b

Table 4.3: Integrated luminosities and number of events for the three samples used in this analysis.

sample. This sample allowed for an unbiased measurement of the ZDC trigger efficiency as discussed in Section 4.6. Because the zero bias trigger does not require any activity in any of the CMS sub detectors, the sample contains very few hadronic collisions. This allowed for a measurement of the electronic noise distributions in the HF, which will be discussed in the next section.

The integrated luminosity for each of the three samples is calculated by recording activity in HF. The cross section for HF activity is measured from a van der Meer scan, and the cross section was found to be X. In this way the amount of integrated luminosity for any period running is related to the activity in HF. An additional method was used to cross check the integrated luminosity obtained by the van der Meer scan technique. The integrated luminosity can also be measured by counting the events that fire the L1 minimum bias trigger together with the inelastic PbPb cross section.

4.3.2 Event selection

The analysis described in this thesis focuses on UPC J/ψs decaying to muons. The trigger used for this analysis recored 346841 events. A set of off-line cuts were applied to increase the relative contribution of UPC events relative to background processes. The following cuts were applied.

Two sets of event selection cuts were applied to reject background events. The first set rejects background from the beam. The second rejects events where hadronic collisions have occurred.

To reject beam induced background the following cuts were applied:

- The reconstructed vertex must be within X cm in the transverse direction and X cm in the longitudinal direction. This cut insures that reconstructed particles come from interactions between the two beams rather than event where one of the two beams interact with gas

cut	cut type	events
all triggered	–	346841
good vertex requirement	beam background rejection	340997
beam halo muon rejection	beam background rejection	302777
cluster shape compatibility requirement	beam background rejection	233590
single-sided neutron requirement	hadronic interaction rejection	149992
two track requirement	hadronic interaction rejection	32732
HF signal rejection	hadronic interaction rejection	5392
muon quality requirement	fake muon rejection	1956
J/ψ mass requirement	kinematic cut	662
muon detectability cuts	kinematic cut	541

Table 4.4: Effects of event selection cuts.

particles near the interaction point.

- Beam halo muons were rejected using the timing of the muon hits. The beam halo cut rejects events where muons surrounding the beam stream through the detector.

- Pixel cluster shape should be compatible with the vertex. This cut requires that energy deposits in the silicon tracker point back to the reconstructed primary vertex.

These beam background cuts do not reject any UPC J/ψ candidates.

The second set of background rejection cuts were designed to reduce contamination from hadronic interactions.

- No more than 2 reconstructed tracks in the event. The track requirement rejects events that produce many charged particles.

- Maximum reconstructed hit energy in HF was required to be below the threshold for electronic noise. Nearly all hadronic interactions ($\sim 98\%$) produce particles in the range $3 < |\eta| < 5$ covered by the HF detector. By requiring that the energy deposits in HF resemble noise, nearly all elastic hadronic collisions are expected to be rejected.

- Energy in the ZDCs consistent with neutrons on only one side of the interaction point. In hadronic interactions both nuclei break-up. By requiring that ZDC only reconstruct neutrons on one side of the interaction point, hadronic interactions that produce neutrons on both sides were rejected.

Each of these cuts are designed to reject topologies produced by hadronic interactions. The effect of these cuts can be seen in TableX.

To establish the HF noise thresholds, the noise distributions were measured in zero bias events. Only presences of both beams was required for these events. An Off-line selection of events with no reconstructed tracks was used insure that no collision had taken place. The noise distribution from this zero bias sample is compared to the physics sample and MC in Fig. 4.1. The HF noise threshold defined as the cut that keeps %99 of the zero bias events.

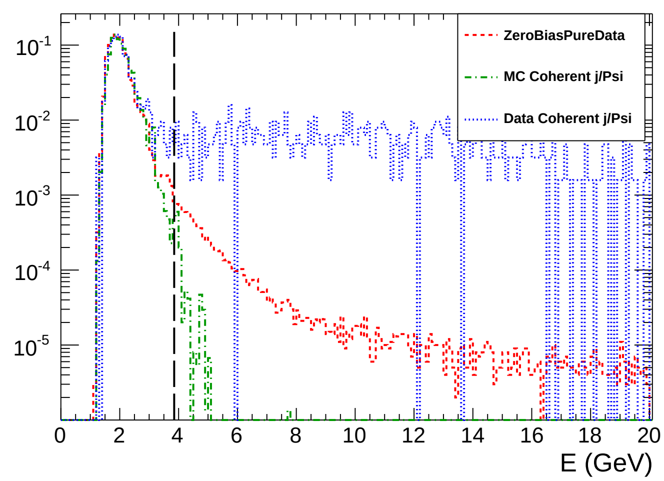

Figure 4.1: Comparison of HF noise distributions in zero bias data, physics triggered data, and MC.

The following standard muon quality cuts are applied:

- Tracker track matched with at least one muon segment (in any station) in both X and Y coordinates ($< 3\ \sigma$).
- Cut on number of tracker layers with hits > 5.
- Number of pixel layers > 0.
- The χ^2 per degrees of freedom of the track fit < 3.

- Loose transverse and longitudinal impact parameter cuts, with in 3 cm in the transverse direction and withing 30 cm in the longitudinal direction with respect to the primary vertex.

These cuts are applied to reduce the number of fake muons.

4.4 Break up determination

4.4.1 ZDC Signal Reconstruction

There are 18 zdc channel. There are 4 hadronic channels and 8 electromagnetic channels on each side of the CMS. To measure neutrons in the ZDC the charge in each channel is first converted to a signal.

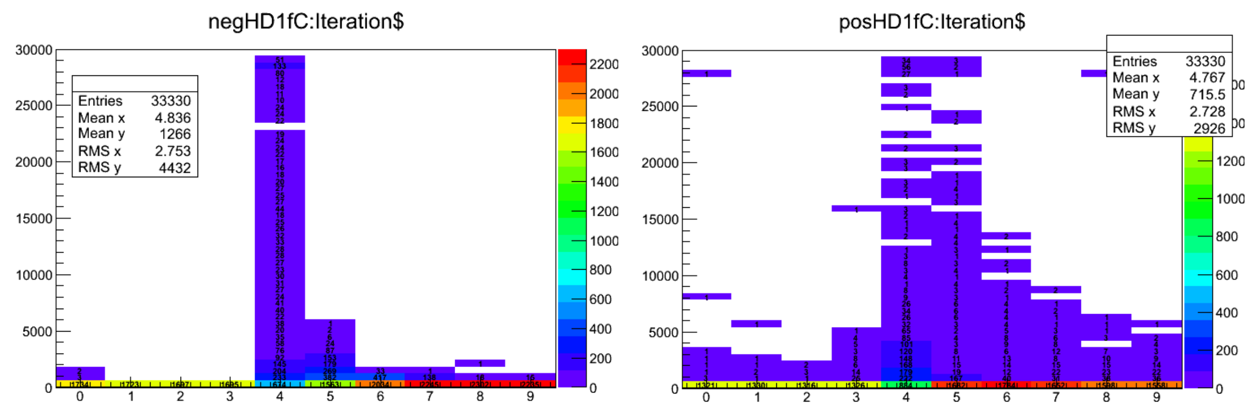

Figure 4.2: ZDC pluse shape.

Channel Signal definition: The signal in the zdc calculated two ways.

1. Method 1
   (a) signal: 4,5,6
   (b) background: 1,2
2. Method 2
   (a) signal: 4

(b) background: 5

As seen in Fig 4.2, method 1 uses all the dominant signal time slices and uses the maximum number of “clean” non signal time slices to estimate the noise pedestal event by event. This minimizes the effect of random noise time slice by time slice by averaging over the maximum number of time slices per event.

Method 2 uses only the two time slice that are most likely to be above zero. Because all signal that is less than zero is not measured, method 1 only allows for a noise pedestal measurement half the time.

The noise spectrum was measured from the pre collisions time slices. Each time slice in Fig. 4.2 is 25 ns in length. In Fig. 4.2 higher than average signal can be seen in the 0th time slice. This is due to events where activity was present in the ZDC for two consecutive bunch crossings, and corresponds to a separation of 200 ns. Time slices 1 and 2 are therefore occurred between colliding bunch crossings. These time slices were used to estimate the noise spectrum.

Fig 4.3 shows the noise spectrum for each of the EM and HAD sections for the two sides of the ZDC. The spectra determined which sections contain only noise.

From these two methods the ZDC+ and ZDC- energy spectra near the one neutron peak are plotted in Fig. 4.4. While method 1 in blue and method 2 in red not differ much in ZDC-, the clear separation of the one neutron peak signal from the noise peak about zero is evident.

4.4.2 Determination of the one neutron thresholds

The ZDC thresholds used to establish the break-up mode were measured from zero bias data. By using this dataset, the spectrum does not contain a trigger bias. The trigger requriment in the event is that both beams were present in CMS. This does however include a significant electronic noise contribution due to events where no neutrons are emitted in the direction of the zdc. To sperate the signal from the electronic noise additional cuts are applied in the zero bias data.

In Fig. 4.2 the pulse shape peaks in the peaks in the fourth time slice, for electronic noise however, any of the ten time slices are equally likely to have a peak value. Using this fact, signal

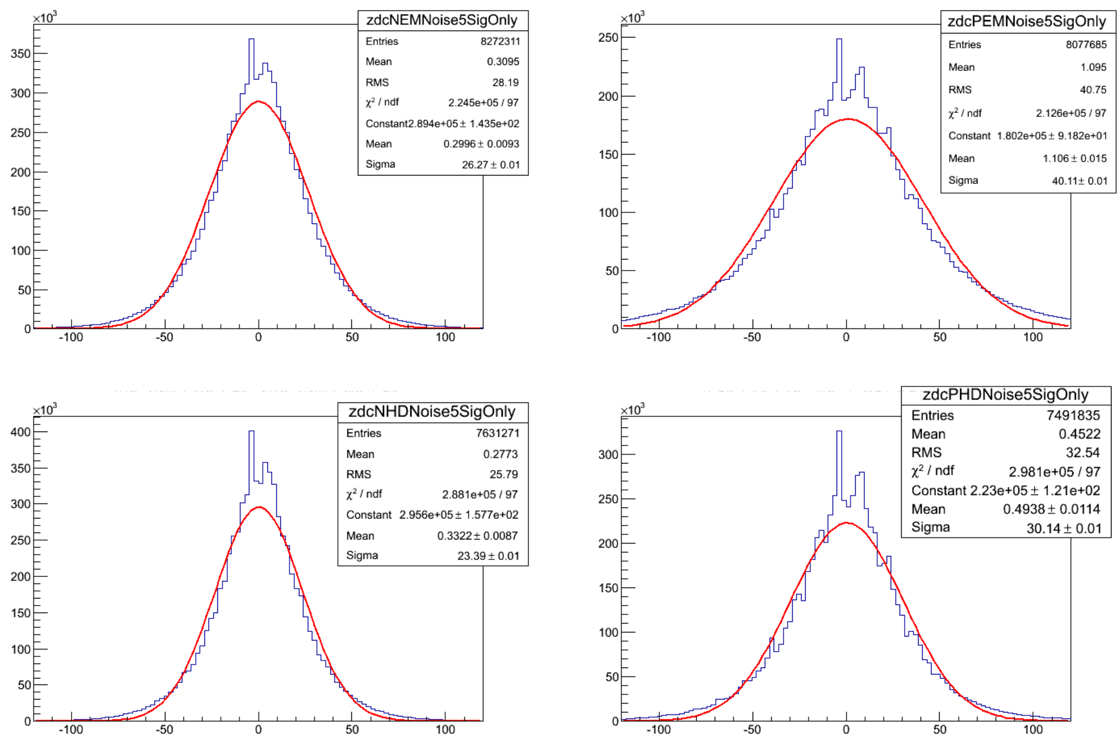

Figure 4.3: ZDC noise spectra from ZDC$^-$ EM section (upper left), ZDC$^+$ EM section (upper right), ZDC$^-$ HAD section (lower left), and ZDC$^+$ HAD section (lower right).

can be preferably selected by requiring that the hadronic channels of the ZDC have a peak signal in the fourth time slice. In Fig. 4.5 no noise subtraction is used. As each additional hadronic channel is required to have a maximum signal in the fourth time slice, the single neutron peak emerges. Using the noise subtraction method described by Method 1, the same signal emerges. Fig. 4.6 confirms that both noise subtraction and the timing require produce the same signal. This gives confidence that the signal is not an artifact of either cut, but the true neutron signal.

Fig. 4.6 and Fig. 4.4 demonstrate the consistence of the using timing cuts and noise subtraction to enhance the signal neutron peak. Fig. 4.6 confirms the legitimacy of the noise subtraction method in ZDC$^-$ by showing the that the same signal emerges from the noise subtraction method as the timing method. Fig. 4.4 demonstrates the corresponds between between noise subtraction method 1 and method 2 on in ZDC$^-$ where signal is better separated from the electronic noise. This allows for confidence that the signal seen in ZDC$^+$ using method 2 is the one neutron peak.

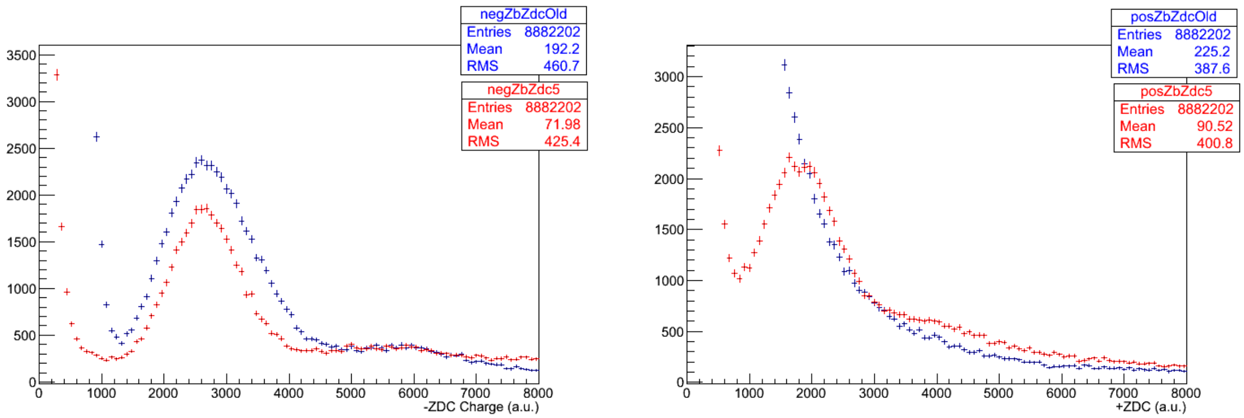

Figure 4.4: Comparison of ZDC signal reconstruction methods.

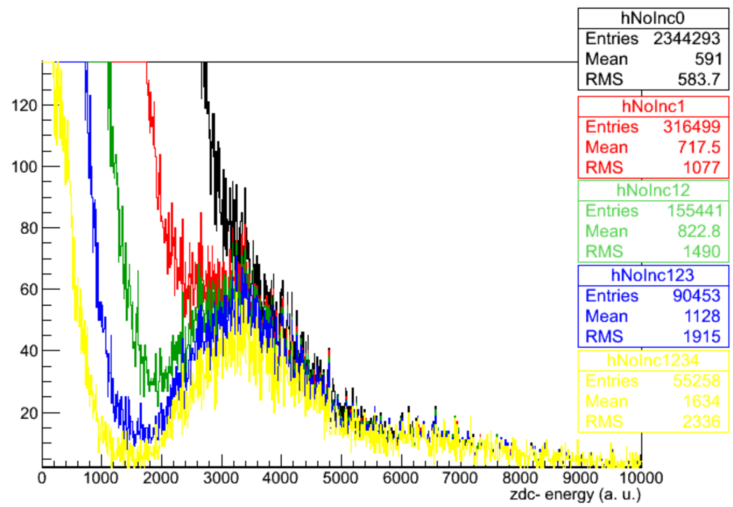

Figure 4.5: Effects of requiring in time signal in ZDC hadronic channels.

The spectrum for method 1 and 2 are fit to a series of Gaussians. The electronic noise is fit to a Gaussian about zero. The one, two, and three neutron peaks are fit Gaussians that are successively broader. The mean of each peak was initially set to multiples of the mean of the one neutron peak. The threshold for a neutron in the ZDC was taken from the fits in Fig. 4.7 and Fig. 4.8. Any signal greater 2 σ below the mean of the one neutron peak was considered signal.

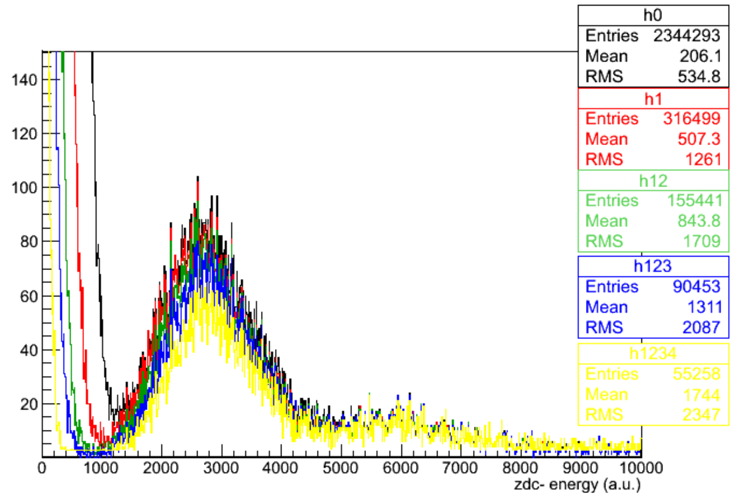

Figure 4.6: Effect of ZDC signal timing requirements after noise subtraction.

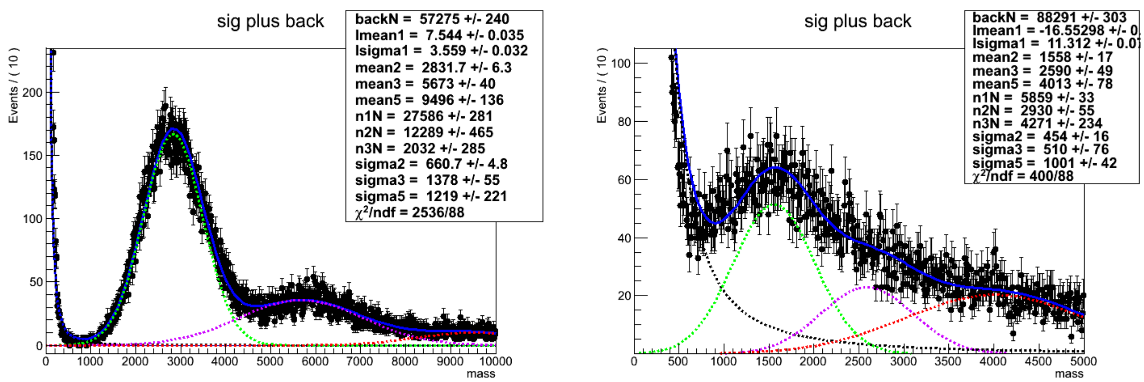

Figure 4.7: Fit to charge spectrum from ZDC$^-$ (left) and ZDC$^+$ (right) using method 1

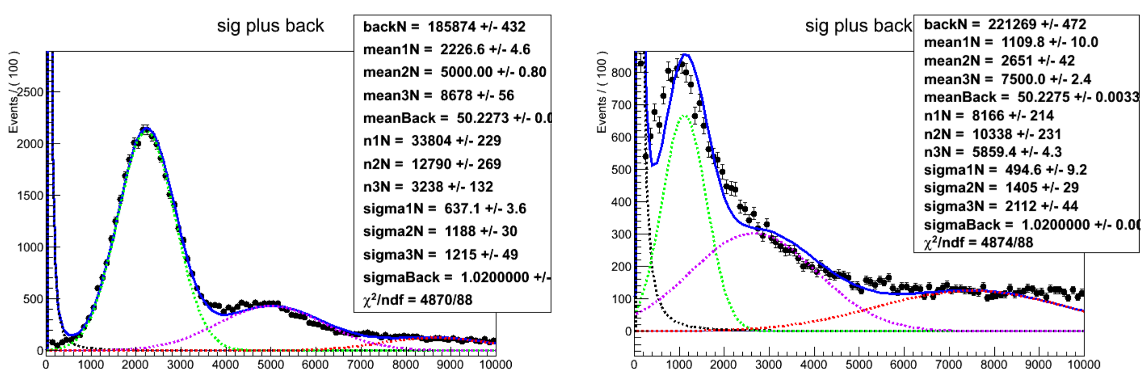

Figure 4.8: Fit to charge spectrum from ZDC$^-$ (left) and ZDC$^+$ (right) using method 2

4.5 Signal extraction

The invariant mass distribution for opposite sign dimuons is shown in Figure 4.9. A J/ψ signal is clearly visible together with tails at higher and lower mass due to the photon-photon process A fit to the invariant mass distribution was done using a Gaussian and a Crystal Ball function to account for the J/psi signal and a first and second order polynomial function for the photon-photon process. The extracted number of J/ψ candidates from this fit includes all J/ψs in the mass window that pass the analysis cuts.

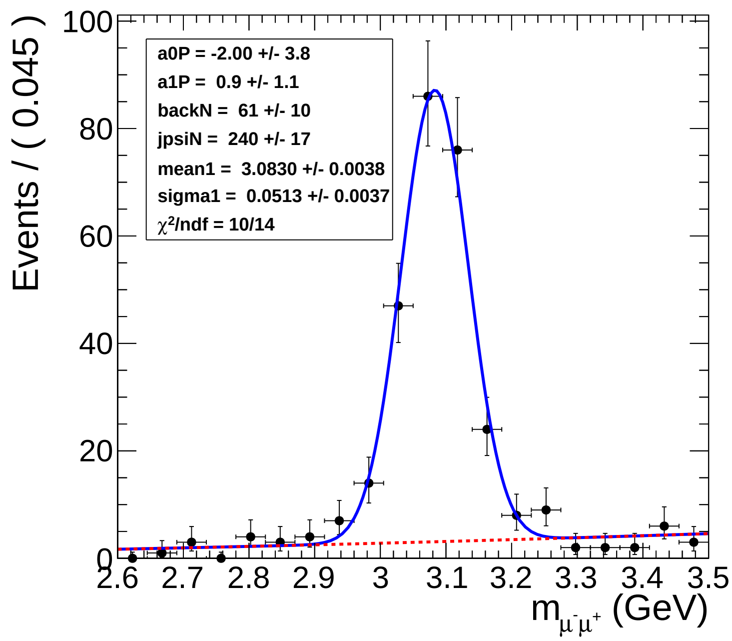

Figure 4.9: Mass fit to J/ψ using Gaussian for the signal and a first order polynomial for the background

The p_T spectrum is fit using templates from the three physics MC samples. These contributions display a different shape in transverse momenta. For this reason, the number of coherent J/ψ candidates were extracted from the dimuon p_T distribution, around the J/ψ mass, after fitting together MC templates for both signal and background. The templates for the fit come form the three STARlight MC samples.

The shape of the photon-photon process and coherent J/ψ are very similar in p_T. These two shapes normalizations are highly anti-correlated in the fit (see Fig. 4.11).

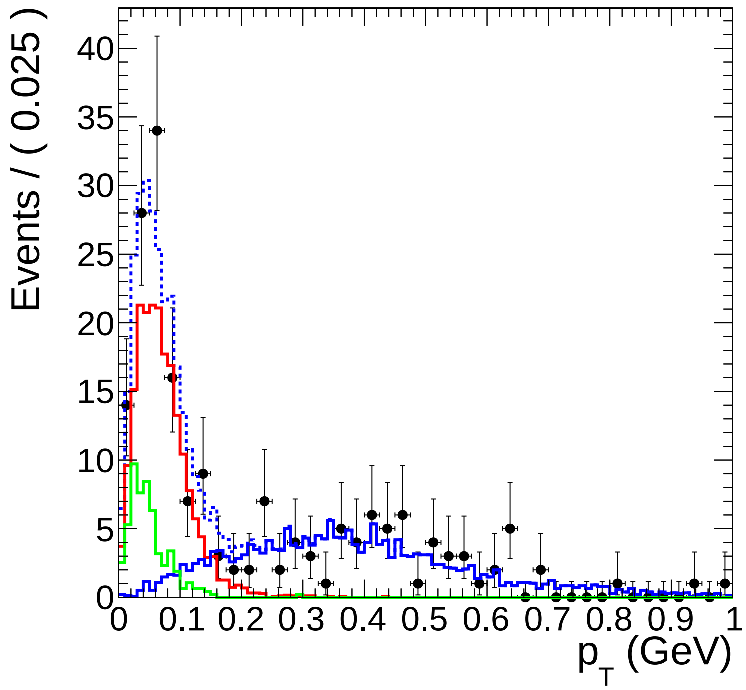

Figure 4.10: Fit to MC p_T templates.

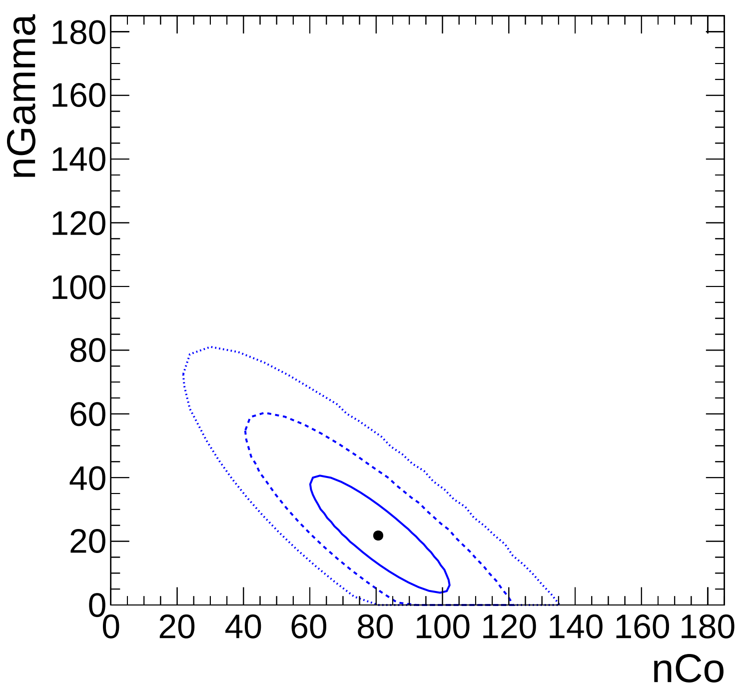

Figure 4.11: 68%, 95%, and 99% confidence contours from the p_T template fit.

To utilize the mass fits ability to distinguish the photon-photon process from the coherent and incoherent process all while utilizing the p_T fits ability to separate the coherent and photon-photon processes from the incoherent, a simultaneous fit to the mass spectrum and p_T spectrum was preformed. In the simultaneous fit, the parameter for the contribution from the photon-photon process is shared by the two fits.

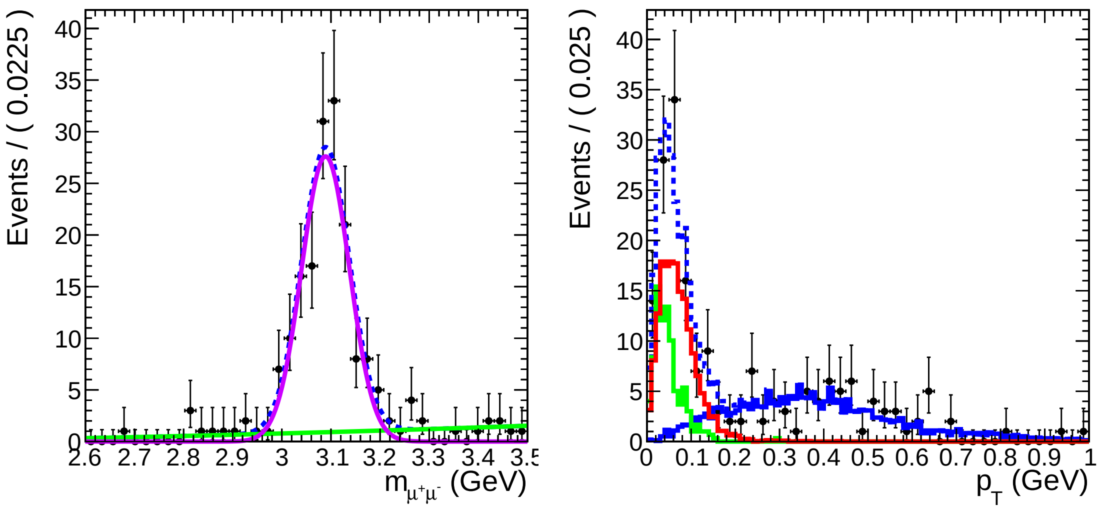

Figure 4.12: Simultaneous fit to the mass and p_T spectra.

By simultaneously fitting both spectra, the anti-correlation between the photon-photon and coherent normalization parameters was reduced as well as the overall error on the parameters. The slope of the confidence contours in Fig. 4.11 and Fig. 4.13 demonstrate the reduction in the correlation between the normalization parameters. The slope in of the confidence contours in Fig. 4.11 is noticeably closer to 0 than the apparent negative slope in Fig. 4.13.

4.6 Efficiency determination

4.6.1 Muon Efficiencies

The muon efficiencies are measured from MC and data. The MC based measurement accounts for the detector acceptance and the efficiency of the muon quality discussed in Section 4.3. The trigger

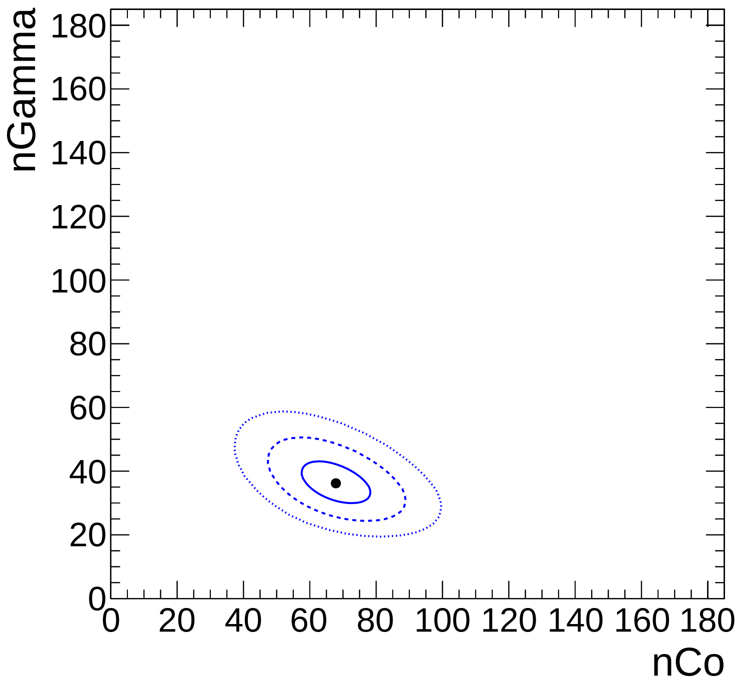

Figure 4.13: 68%, 95%, and 99% confidence contours from the simultaneous fit.

efficiencies were measured in data using the tag and probe method, which is discussed below.

CMS has a limited acceptance for J/ψs, particularly in the case of J/ψs with low momentum like those produced in UPC events. To measure the acceptance of CMS for J/ψs, reconstructed dimuon candidates were considered detectable if both reconstructed daughters fell into a detectability region. This region was defined using the coherent J/ψ events obtained from STARlight. The efficiency for reconstructing single muons ε^{μ}_{reco} is defined by $\varepsilon^{\mu}_{reco} = \frac{N^{\mu}_{reco}}{N^{\mu}_{gen}}$, where N^{μ}_{reco} is the number reconstructed muons after after the full CMS detector simulation and that pass the standard muon quality cuts, and N^{μ}_{gen} is the number of generated muons from STARlight. Fig. 4.14 shows the efficiency for reconstructing single muons from coherent J/ψ events. To avoid the edges of the detectors acceptance, all reconstructed muons that fall into a (p_T,$|\eta|$) bin that has an efficiency less than 20% were rejected thus defining the detectability region. The acceptance for reconstructing dimuons was calculated from MC using the following formula:

$$A = \frac{N_{det}(|y|, p_T)}{N_{gen}(|y|, p_T)}, \tag{4.1}$$

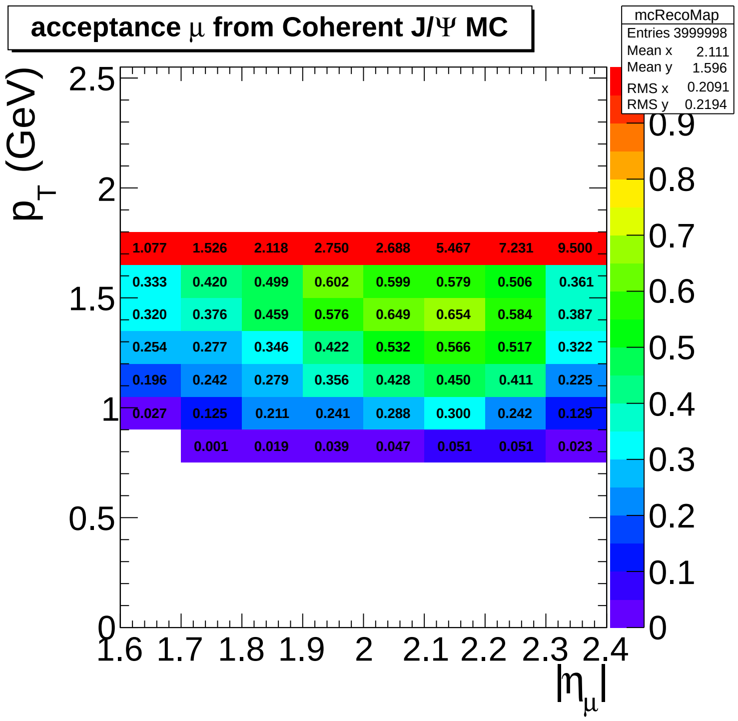

Figure 4.14: Muon daughter detectability from coherent J/ψ, incoherent J/ψ, photon-photon, and J/ψ gun samples.

where N_{det} is the number of reconstructed dimuons where both daughters fall in to the detectability region, and N_{gen} is the number of generated dimuons. From Eq. 4.1, the acceptance for J/ψ was calculated as a function of $|y|$, and p$_T$ (see Fig. 4.15).

The tag and probe method is used to measure the trigger efficiency of the muon daughters, which is a data driven approach. In this method there are three categories of daughter muons. Tag muons are high quality muons. Passing probes are reconstructed muons that match the muon trigger, while failing probes do not. Each dimuon will have one daughter classified as a tag and the other as a probe. From here three invariant mass histograms are studied. One histogram is created from all pairs. The second comes from pairs where the probe is a passing probe. The last histogram comes from pairs where the probe fails to fulfill the trigger, *i.e.* the probe is a failing probe. Because this depends on the p$_T$ and $|\eta|$ of the probe, one set of three histograms for each (p$_T$,$|\eta|$) bin of the probe is created.

To extract the single muon trigger efficiency ε^{μ}_{trig}, each set of invariant mass histograms was

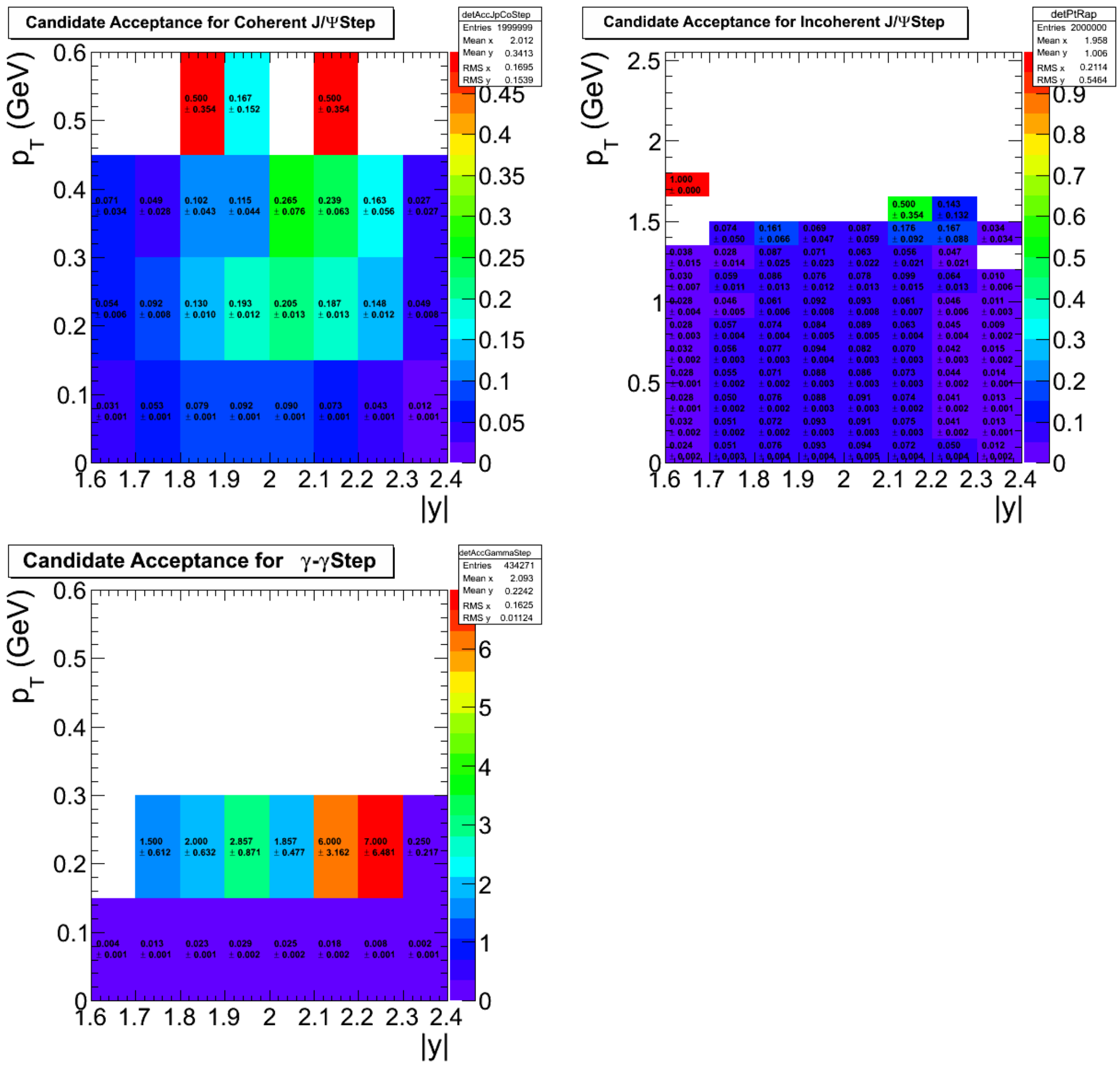

Figure 4.15: Dimuon acceptance from coherent J/ψ (top left), incoherent Jψ (top right), and photon-photon interactions (lower).

simultaneously fitted. The signal was fitted using a Crystal Ball function, and the background was fitted to an exponential. The Crystal Ball parameters were simultaneously fitted to all three histograms. The exponential function was fitted to the failing and passing probe histograms separately. Because the background shapes are in principal different for the two samples, the efficiency is driven by this difference.

To measure the trigger efficiency a tag is required to pass all muon quality cuts and matched to the trigger. The probe is required to pass all quality cuts. A passing probe is a probe that is also matched to the trigger. In this way the tag leaves the probe in biased by the trigger and the efficiency can be measued by fitting mass.

Fig. 4.16 shows the fit of the three sets of pairs. This fit is done for each bin of the probes p_T

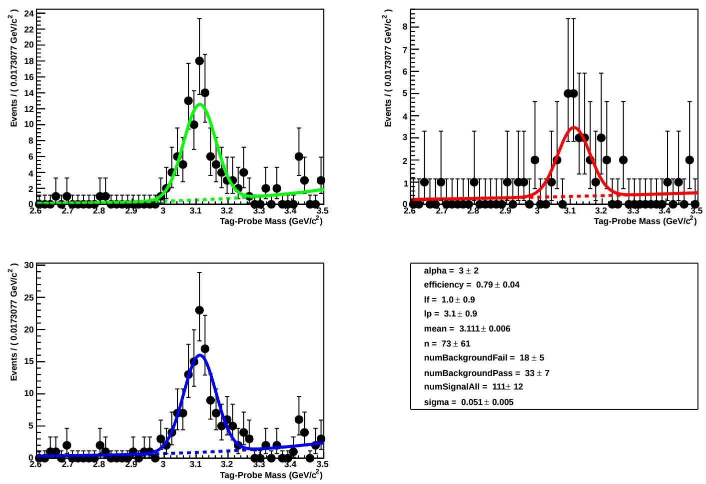

Figure 4.16: Fits to tag and probe pairs in the J/ψ mass region.

and η. The resulting fit is in Fig. 4.17.

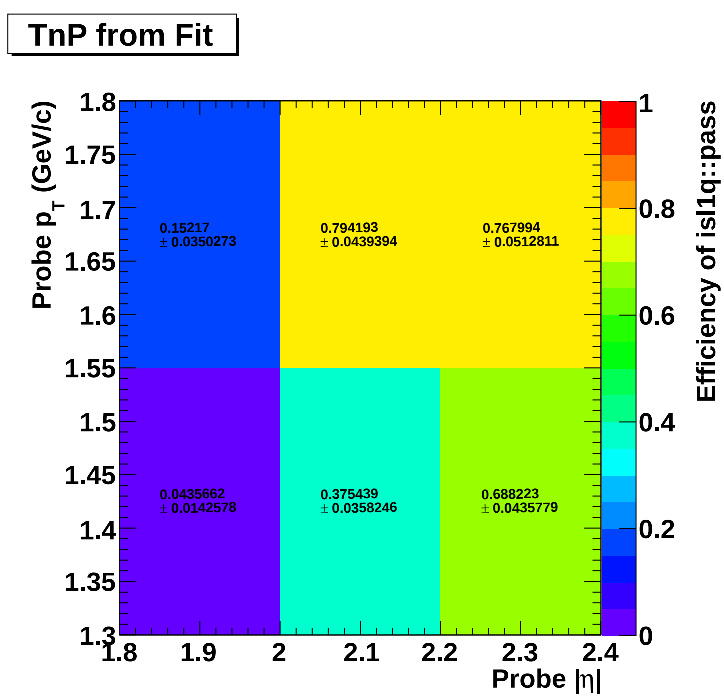

Figure 4.17: Muon trigger efficiencies in p_T and η bins from the tag and probe method.

The dimuon trigger efficiency $\varepsilon_{dimuontrigger}$ was measured from the single muon efficiencies. The efficiency of each candidate was calculated using the following equation:

$$\varepsilon_{dimuontrigger} = 1 - (1 - \varepsilon^{\mu_1}_{trigger})(1 - \varepsilon^{\mu_2}_{trigger}), \tag{4.2}$$

where $\varepsilon^{\mu_1}_{trigger}$ is the tag and probe efficiency of the first dimuon daughter, and $\varepsilon^{\mu_2}_{trigger}$ is the efficiency of the second muon daughter. In Eq. 4.2 the probability of at least one daughter firing the trigger is calculated by subtracting one from the probability that neither daughter fires the trigger, thus giving the dimuon trigger efficiency.

The average dimuon trigger efficiency for each dimuon (p$_T$,$|y|$) bin was calculated by averaging the individual dimuon candidates in each bin. The average trigger efficiency was multiplied by

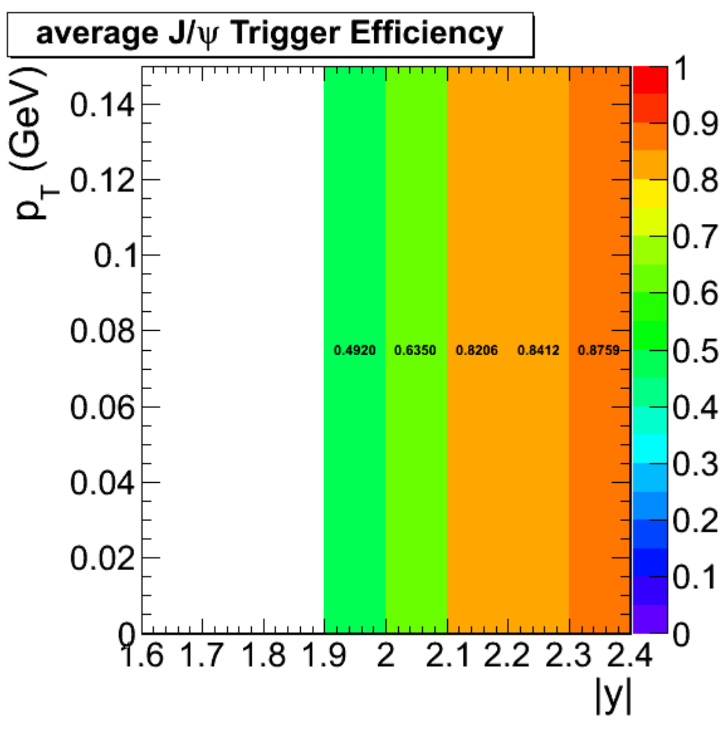

Figure 4.18: The trigger efficiency from tag and probe averaged over candidates in each (p$_T$,$|y|$) bin.

the acceptance from the MC to produce a total efficiency times acceptance factor.

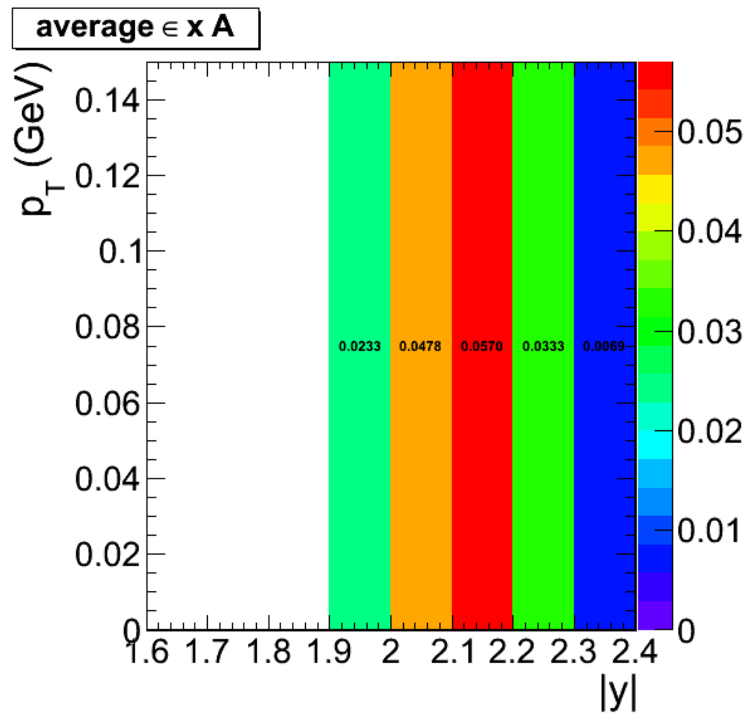

Figure 4.19: The acceptance times averaged trigger efficiency from tag and probe.

4.6.2 ZDC trigger efficiency

A special trigger was prepared to monitor the ZDC trigger efficiency. This trigger required either a ZDC^+ or ZDC^- trigger, together with at least one pixel track. Events were accepted offline if there was no activity in the BSCs or activity on a single side. This sample suffers from a trigger bias. For example, a sample triggered by ZDC^+ would always produce a ZDC^+ trigger efficiency of one. To avoid this, the special trigger sample was divided into two subsamples in the following way. A first sample triggered by the ZDC^+ input and second one triggered by the ZDC^-. The ZDC^+ trigger efficiency is measured from the ZDC^- sample, and vice versa.

The trigger efficiency for reconstructed ZDC energies above the single neutron threshold were estimated (see for Sec. 4.4). The ZDC^+ efficiency was calculated using the ZDC^- triggered sample. To estimate the efficiency, the number of events with energy in ZDC^+ greater than the single neutron threshold, N_{events}, were measured. From this set of events, the number of events that also fire the ZDC^+ are measured. The ratio between the number of single neutron events that fire the trigger and all single neutron events was taken as the estimate of trigger efficiency. The same

ZDC Side	Reco Method	N_{events}	N_{trig}	ε_{ZDC}
ZDC^+	1	72946	71688	0.982 ± 0.005
ZDC^+	2	73028	71706	0.9819 ± 0.005
ZDC^-	1	76137	71786	0.9429 ± 0.005
ZDC^-	2	76132	71859	0.9439 ± 0.005

Table 4.5: ZDC trigger efficiencies for ZDC reconstruction method 1 and 2

procedure is applied for each side of the ZDC.

4.7 Systematic checks

4.7.1 HF noise threshold

The way in which the HF noise distribution is measured effects the events selection. In Table 4.4 the importance of cutting on HF noise is evident. The HF cut requires signal consistent with noise and in turn rejects hadronic events. The HF noise cut rejects X of the events that remaining. The systematic uncertainties on the HF noise requirement is important for this reason. The result must not depend significantly on the method used to apply the cut on the noise because of the large reduction of events that result from it.

Four different approaches were employed to estimate the systematic effect arising from pick a particular method. By looking at the variation of the number of events that remain after applying the thresholds derived from these four methods, the systematic uncertainty for the HF noise cut was estimated. The four methods are derive from combinations of two variations. The type of object was varied from a low-level detector object called a RecHit to a higher level physics object called a CaloTower. The distinction between the two is that the RecHit is the energy deposited in a single calorimeter detector element, where as the CaloTower is a collection of RecHits with varrious threholds, which represent a full energy deposit that would come from a particle or a collection of particles from a jet passing through the detector. The second variation is on the separation of the two sides. In one case the threshold is derived for the two sides combined. In another case the thresholds are calculated separately for the two sides of HF. By combining these two variations a total of four estimates of the effect of the HF noise cut were made. Table 4.6 below shows the thresholds that are measured for each of the four methods. The resulting yields from the four different methods are displayed in Table 4.7.

Object type	HF (GeV)	HF^{-} (GeV)	HF^{+} (GeV)
RecHits	3.85	3.25	3.45
CaloTowers	4.25	3.25	3.75

Table 4.6: HF noise theresholds for various noise measurement methods.

Object type	Combinded HF threshold	Two-sided thresholds
RecHits	298	290
CaloTowers	302	288

Table 4.7: Candidate yields below 1.05 GeV p_T for various HF noise cuts.

The threshold was adjusted to estimate the effect of tightening the requirement on the zero bias data. By requiring successively lowering the percentage of the zero bias sample that was included, the HF noise cut was made more restrictive including less first 98%, than 97% of all zero bias events. This allows for an estimate of the systematic uncertainty on selecting a 99% cut. Table 4.8 shows the effect on the thresholds themselves for both RecHits and CaloToweres, whereas Table 4.9 shows the effect on the candidate yields.

Table 4.8: Values of the energy cuts for the HF calorimeter for RecHit and CaloTower in GeV.

%	E_{RecHit} GeV	$E_{CaloTower}$ GeV
99	3.85	4.25
98	3.25	3.75
97	2.95	3.25

4.7.2 MC vs Data compairson

4.7.3 Tag and probe

To estimate the effect the tag and probe fits, the tag and probe efficiencies were additionally measured by counting probes in the J/ψ mass window.

Table 4.9: Number of dimuon candidates with p_T <1.05 when changing HF calorimeter cuts for RecHit and CaloTower.

%	RecHit cut	CaloTower cut
99	298	302
98	287	294
97	284	280

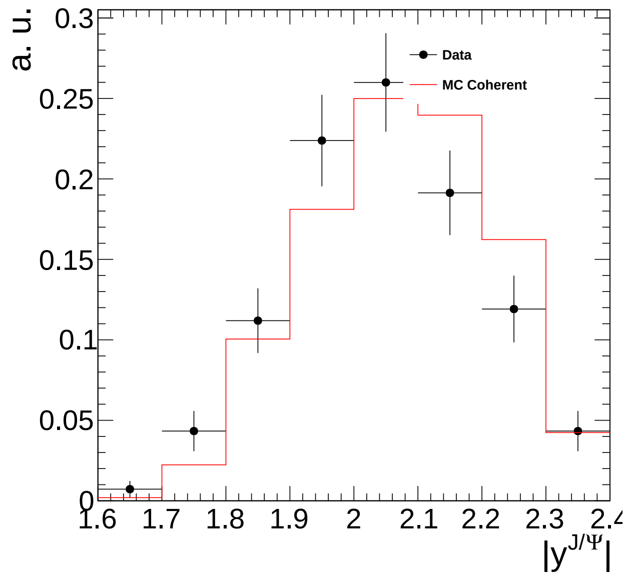

Figure 4.20: Comparison of the of the dimuon rapidity distributions between coherent MC sample and Data.

4.7.4 Template fit

The normalization for the coherent and incoherent templates are left free. To address this issue the template from the photon-photon process was fixed to the cross section value given by STARlight and normalized to the integrated luminosity of the data. The normalization for the photon-photon template was allowed a range of 20% due to the 20% uncertainty in the STARlight cross section.

The systematic uncertainty for the contribution to the three components of the signal was estimated by varying the mass fit. Because the mass fit is used to fix the contribution to the p_T spectrum of the photon-photon process, the change of the mass fit results in different coherent contributions from the p_T template fit.

Moving from left to right in Fig 4.25 the contribution from the photon process increases. The

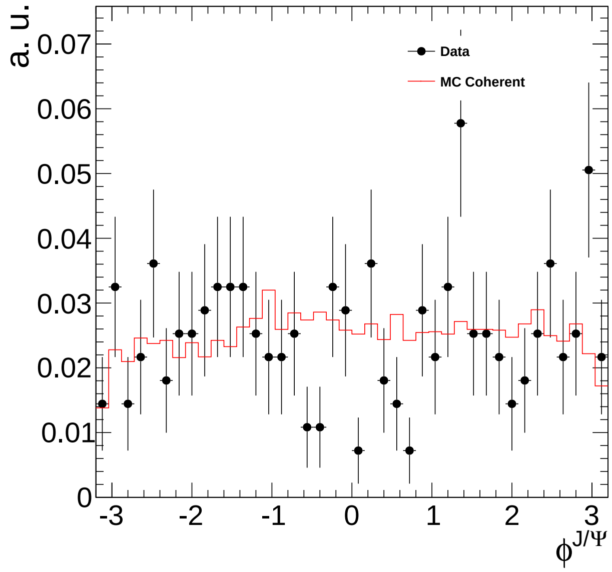

Figure 4.21: Comparison of the of the dimuon φ distributions between coherent MC sample and Data.

left most fit uses a Crystal Ball function to account for the radiative decay of the final state daughters of the J/ψ. The low mass exponential portion however picks up background events and overestimates the J/ψ contribution. The right most plot fits the background to a 2nd order Cheby-Chev polyinomial, which overestimates the background. Because the Cheby-Chev peaks just below the J/ψ peak, this fit overestimates the background and in turn underestimates the signal contribution. The Gaussian fit with a linear background however does a reasonable job of fitting both the background and the signal.

From these three fits an upper and lower bound of the systematics due the choice of fit functions was estimated.

4.7.5 Mass fit

Fig. 4.26 demonstrates the small dependence the raw J/ψ yield has on the fitting function. Both fit functions agree well, with reduced χ^2 values below one. The Crystal ball fit give an upper estimate for the J/ψ yield. The Gaussian fit gives an lower estimate. The main difference comes from the lower mass tails. In the Crystal ball fit the lower tail is considered to be signal due to shifting of

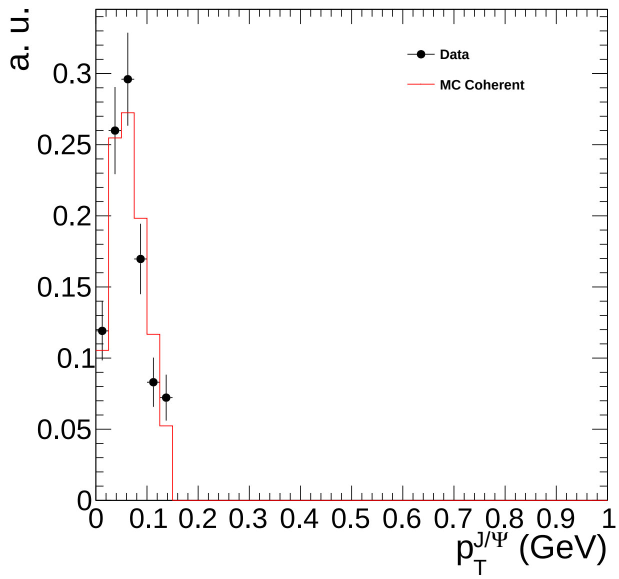

Figure 4.22: Comparison of the of the dimuon p_T distributions between coherent MC sample and Data.

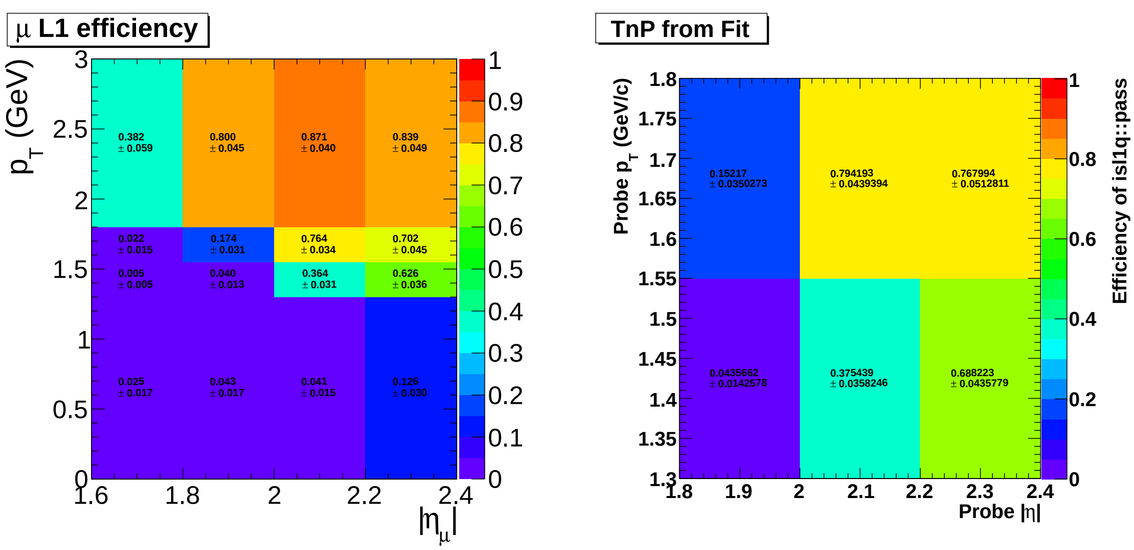

Figure 4.23: Tag and probe trigger efficiencies from counting (left) compared to fitting (right)

the mass spectrum to lower mass due to radiation from the final state muons. In the Gaussian fit the lower mass tail is considered to be background and the signal is sharper.

As check on the simultaneous p_T and mass fit, the mass fit is done using mass templates from STARlight.

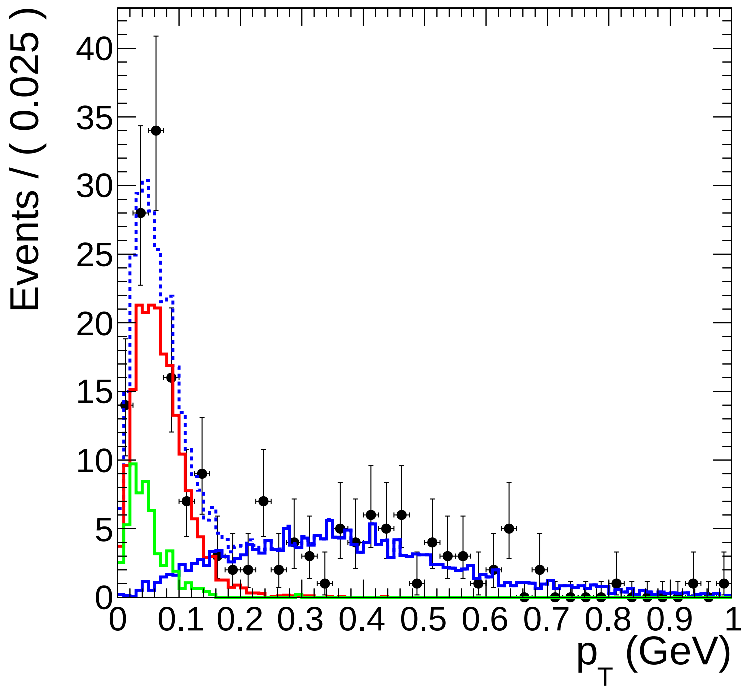

Figure 4.24: Coherent, incohernt, and photon-photon process p_T template fit to data.

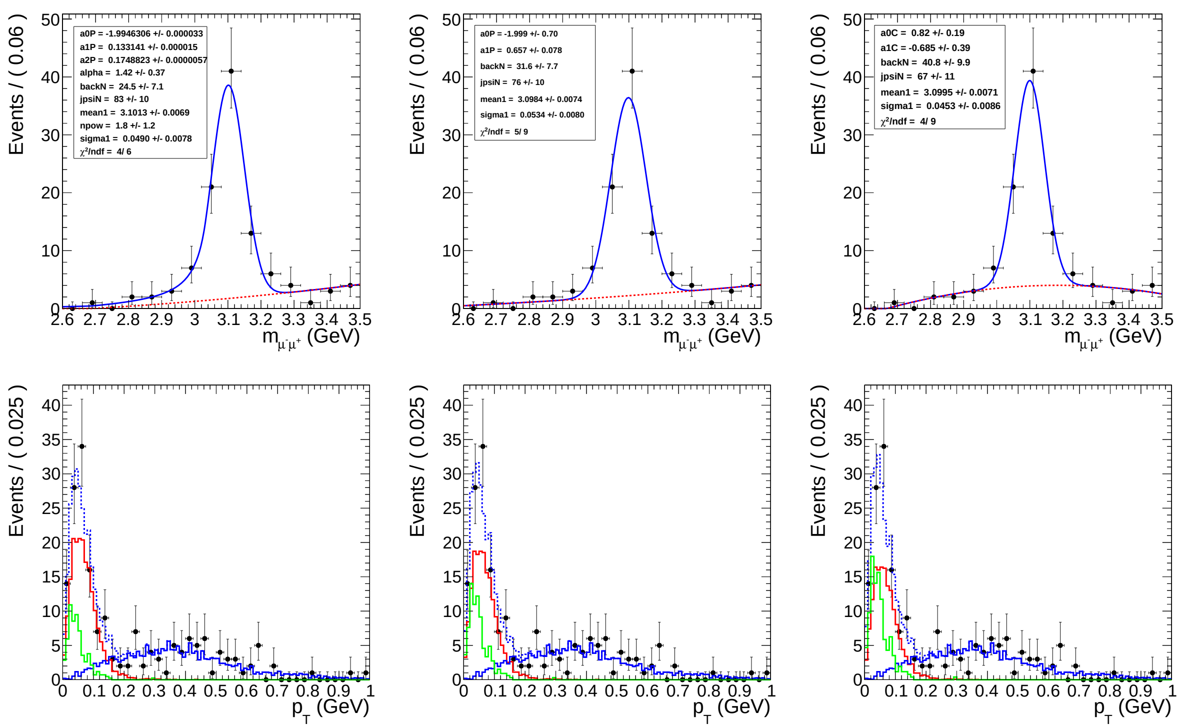

Figure 4.25: Various mass distribution fits and the corresponding p_T template fit.

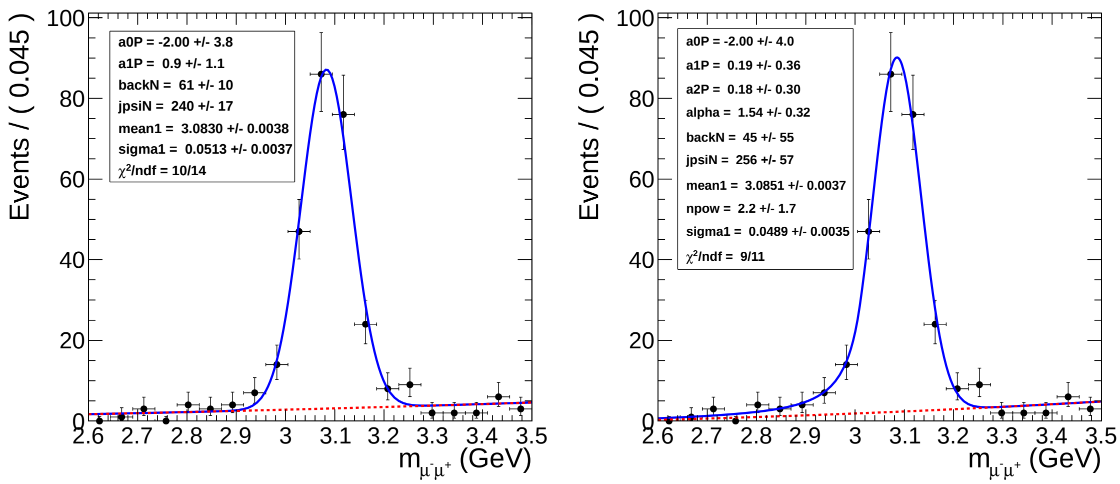

Figure 4.26: Mass fit to J/ψ using Gaussian (Left) and Crystal Ball (Right) for the signal and a polynomial for the background

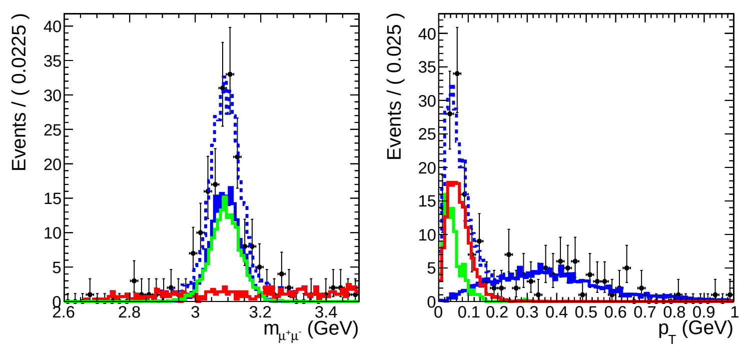

Figure 4.27: Simultaneous fit to the mass and p_T using mass templates for the mass fit.

4.7.6 MC acceptance

To estimate the effect of the GEN level p_T distribution on the acceptance the incoherent sample was used to correct the coherent yield.

The effect of polarization was estimated by correcting by the acceptance for an polarized J/ψ sample.

4.7.7 ZDC efficiency

To estimate systematic errors in the ZDC trigger efficiency, the trigger efficiency was measured from five additional samples.

ZDC Side	Reco Method	N_{events}	N_{trig}	ε_{ZDC}
(ZDC^{+} or ZDC^{-}) and 1 pixel track				
ZDC^{+}	1	72946	71688	0.982 ± 0.005
ZDC^{+}	2	73028	71706	0.9819 ± 0.005
ZDC^{-}	1	76137	71786	0.9429 ± 0.005
ZDC^{-}	2	76132	71859	0.9439 ± 0.005
(ZDC^{+} or ZDC^{-})				
ZDC^{+}	1	30986	30333	0.9789 ± 0.0079
ZDC^{+}	2	31029	30339	0.9778 ± 0.0079
ZDC^{-}	1	39178	30164	0.7699 ± 0.0059
ZDC^{-}	2	35703	30443	0.8527 ± 0.0067
Zero Bias				
ZDC^{+}	1	109967	101598	0.9239 ± 0.0040
ZDC^{+}	2	110230	101561	0.9214 ± 0.0040
ZDC^{-}	1	253241	86660	0.3422 ± 0.0013
ZDC^{-}	2	156336	87401	0.5591 ± 0.0024
Zero Bias with ZDC timing cuts				
ZDC^{+}	1	88676	84429	0.9521 ± 0.0046
ZDC^{+}	2	88480	84202	0.9517 ± 0.0046
ZDC^{-}	1	59878	54728	0.9140 ± 0.0054
ZDC^{-}	2	60467	54733	0.9052 ± 0.0053
(ZDC^{+} or ZDC^{-}), 1 pixel track, and L1 Muon trigger				
ZDC^{+}	1	65466	63376	0.9681 ± 0.0054
ZDC^{+}	2	65543	63358	0.9667 ± 0.0054
ZDC^{-}	1	71929	63512	0.8830 ± 0.0048
ZDC^{-}	2	72932	63582	0.8718 ± 0.0047
(ZDC^{+} or ZDC^{-}), 1 pixel track, and L1 EG trigger				
ZDC^{+}	1	613758	602123	0.9810 ± 0.0018
ZDC^{+}	2	614014	601863	0.9802 ± 0.0018
ZDC^{-}	1	643905	602671	0.9360 ± 0.0017
ZDC^{-}	2	647888	603089	0.9309 ± 0.0017

Table 4.10: ZDC trigger efficiencies for ZDC reconstruction method 1 and 2 for different trigger samples

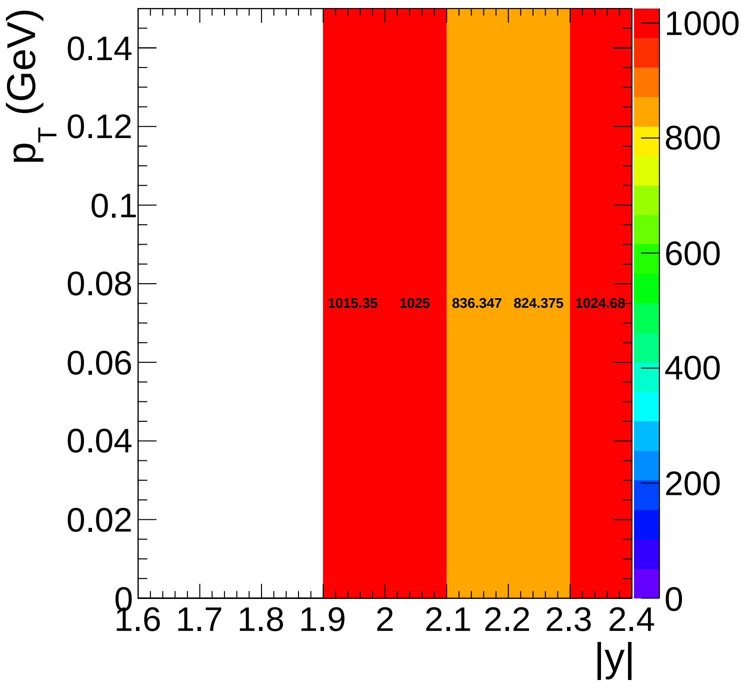

Figure 4.28: Yields corrected by the MC incoherent acceptance map.

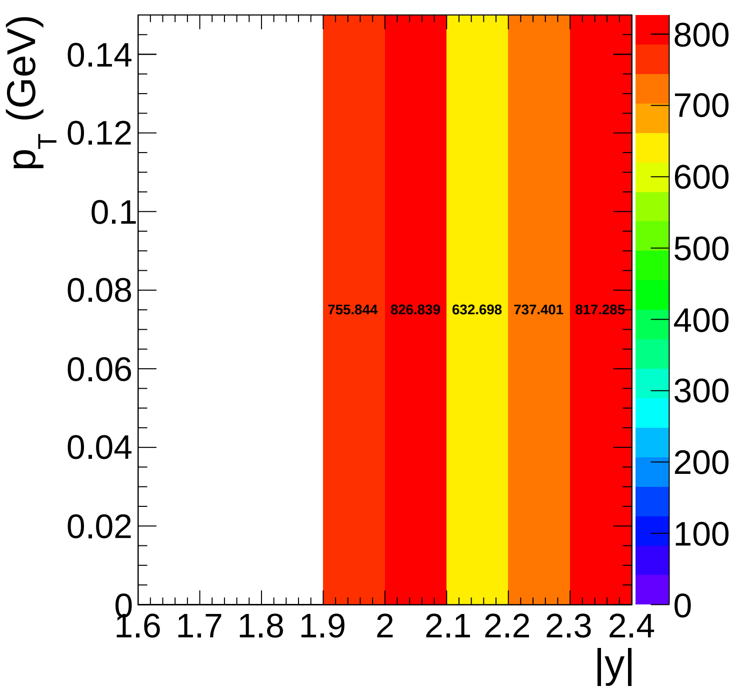

Figure 4.29: Yields corrected by an unpolarized J/ψ sample.

Chapter 5

Results

5.1 Coherent cross section

For the coherent cross section, the raw yield of dimuon candidates was measured after applying the cuts described in Section 4.3.

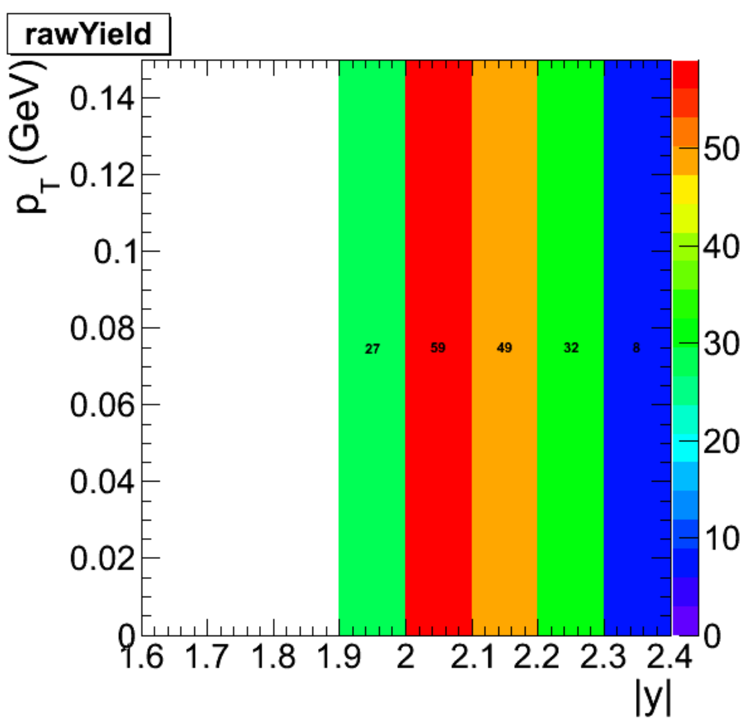

Figure 5.1: Raw yield for the Coherent cross section measurement.

The raw yields were divided by the total efficiency times acceptance factors to produce corrected yields.

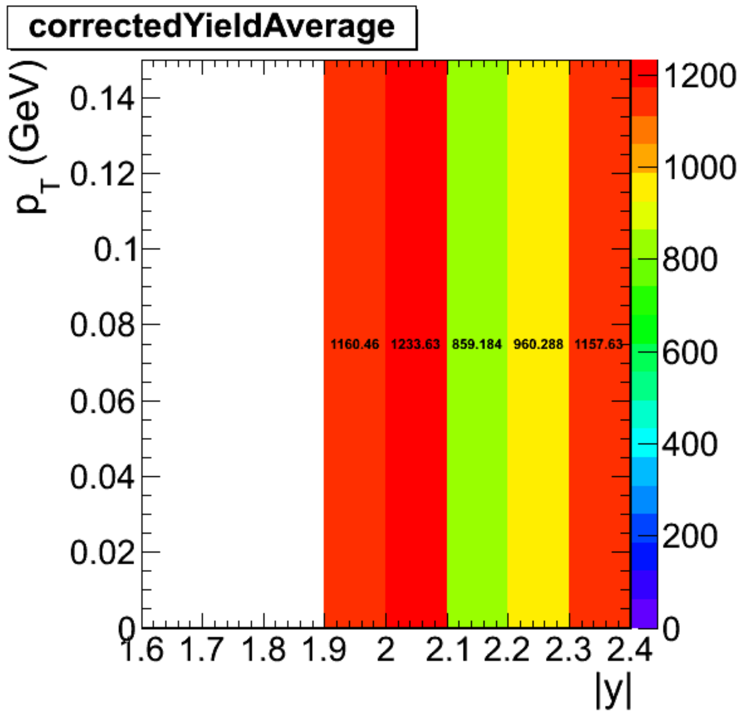

Figure 5.2: Corrected yields for the coherent p_T region.

The corrected yields in the 2.0-2.1 and 2.1-2.2 $|y|$ rapidity bins were added together to calculate the cross section. These bins were selected to insure a total acceptance times efficiency greater than 5%.

The contribution from coherent production was estimated from the template fit in Fig. 4.24. The first three bins are used to estimate the contribution below 150 MeV.

5.2 Incoherent cross section

5.3 Break up ratios

In Table 5.3 the ratio between raw yields for different break up modes are shown.

Fig. 5.3 and Fig. 5.4 compare the raw break up ratios two STARlight and LTA predictions.

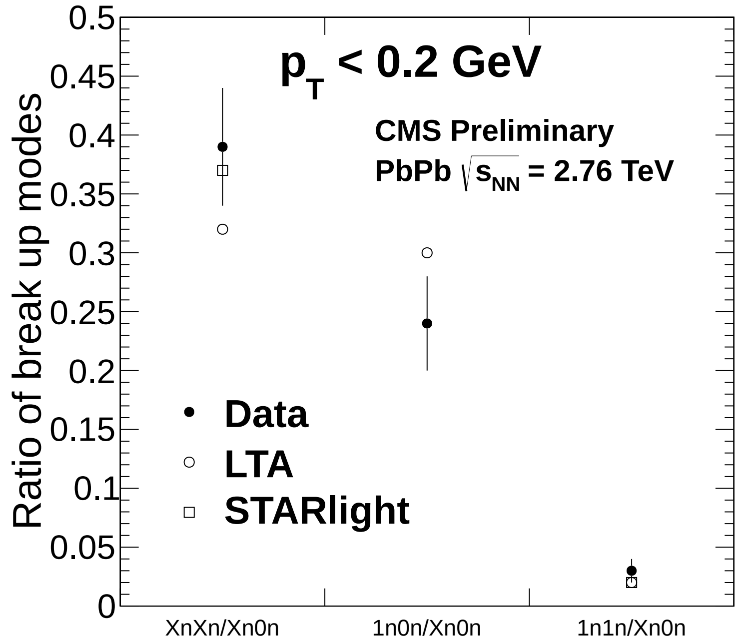

Figure 5.3: Ratio between J/ψ yeilds XnXn and 1n0n break-up modes compared the Xn0n break-up mode for J/ψ with p_T below 150 MeV.

In Table 5.1 the ratio between break up modes are shown for different theories and processes.

Table 5.1: Number of J/ψ integrated over p_T and y with statistical uncertainty.

	X_nX_n/X_n0_n	$1_n0_n/X_n0_n$	$1_n1_n/X_n0_n$
STARlight coherent	0.37	-	0.02
Zhalov coherent	0.32	0.30	0.02
STARlight incoherent	0.37	-	0.007±0.02

5.4 diMuon-neutron correlations

The invariant mass distribution for different break-up modes is show for the coherent and incoherent J/ψ on the Fig. 5.5 and Fig. 5.6 respectively.

The number of the coherent and incoherent J/ψ for each break-up mode are given in the Tab. 5.2. The ratios between the modes X_nX_n, 1_n0_n, 1_n1_n and the mode X_n0_n are given in the table Tab. 5.3. Some of the ratios can be obtained from STARLIGHT and from the Zhalov and thus

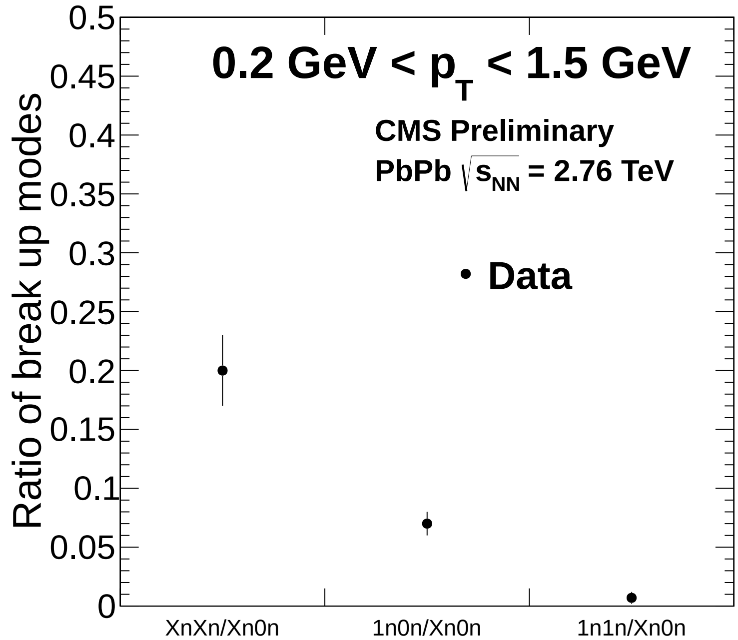

Figure 5.4: Ratio between J/ψ yeilds XnXn and 1n0n break-up modes compared the Xn0n break-up mode for J/ψ with $0.2 < p_T < 1.5$ GeV.

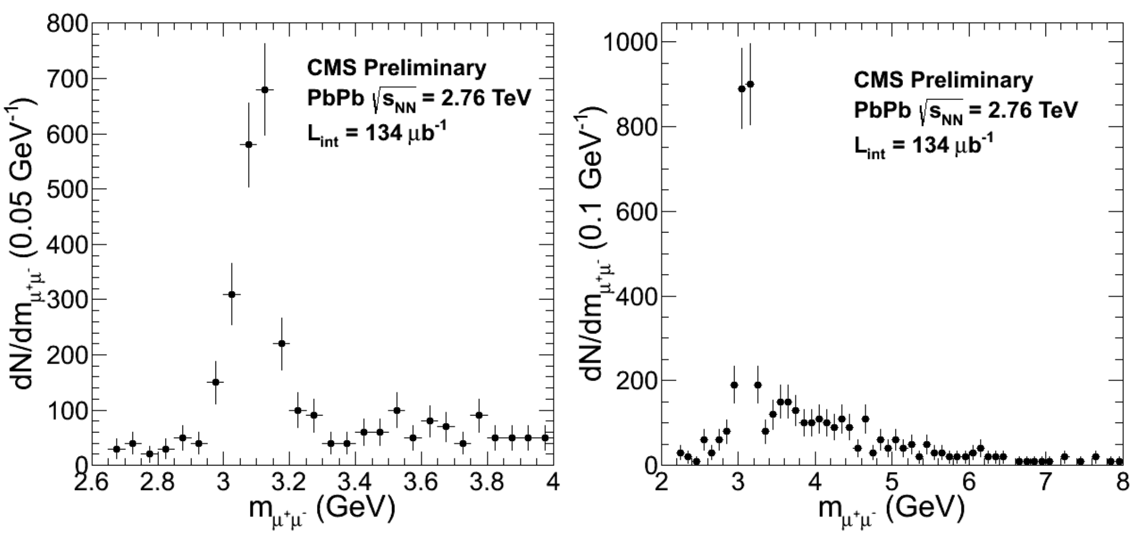

Figure 5.5: Invariant mass spectrum of the opposite signs di-muons originating from the coherent J/ψ for X_n0_n breakup mode for two invariant mass regions.

are given in Tab. 5.1.

For statistical reason, further studies concentrate only on the break-up mode X_n0_n.

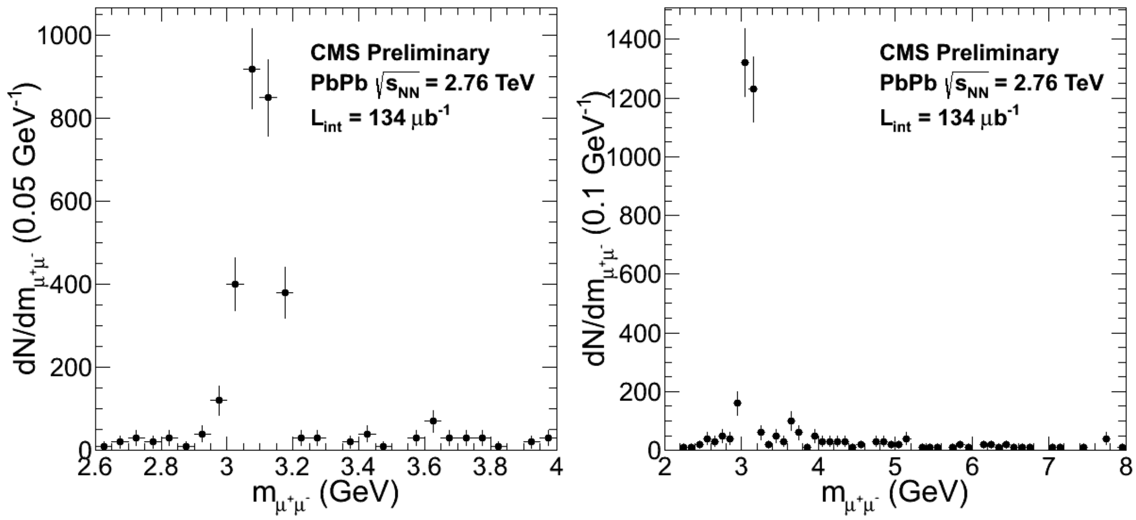

Figure 5.6: Invariant mass spectrum of the opposite signs di-muons originating from the incoherent J/ψ for X_n0_n breakup mode for two invariant mass regions.

Table 5.2: Number of coherent J/ψ integrated over p_T and y with statistical uncertainty.

	X_n0_n	X_nX_n	1_n0_n	1_n1_n
coherent J/ψ	242±16	94±10	58±8	8±3
incoherent J/ψ	291±17	57±8	19±4	2±1

Figure 5.7 shows the transverse momentum distribution of the J/ψ (coherent and incoherent) in the case when J/ψ and neutron have the same or opposite rapidity direction. The ratio between the J/ψ and neutron that have the opposite direction and the J/ψ and neutron that have the same direction i shown on Fig. 5.8. The red curve gives the pure theory calculations, the black one gives the theory results that are injected to the detector simulation and thus taking into account experimental bias.

The rapidity distributions of the coherent and incoherent J/ψ are shown in the Fig. 5.9. They are shown separately for the events firing the ZDC$^+$ and ZDC$^-$. The same distributions are also obtained for the MC and shown in Fig. 5.10. For the MC the particle gun generator with the input p_T spectrum from Zhalov's calculation (LTA). The rapidity symmetry for coherent J/ψ and asymmetry for incoherent J/ψ are observed in data and MC. These are quantified in the Tab. 5.4.

Table 5.4 gives the number of coherent and incoherent J/ψ separately for the events that fired the ZDC$^-$ and ZDC$^+$. We quote separately the J/ψ that have the same or opposite rapidity direc-

Table 5.3: Number of coherent J/ψ integrated over p_T and y with statistical uncertainty.

	X_nX_n/X_n0_n	$1_n0_n/X_n0_n$	$1_n1_n/X_n0_n$
coherent J/ψ	0.39±0.05	0.24±0.04	0.03±0.01
incoherent J/ψ	0.20±0.03	0.07±0.02	0.007±0.005

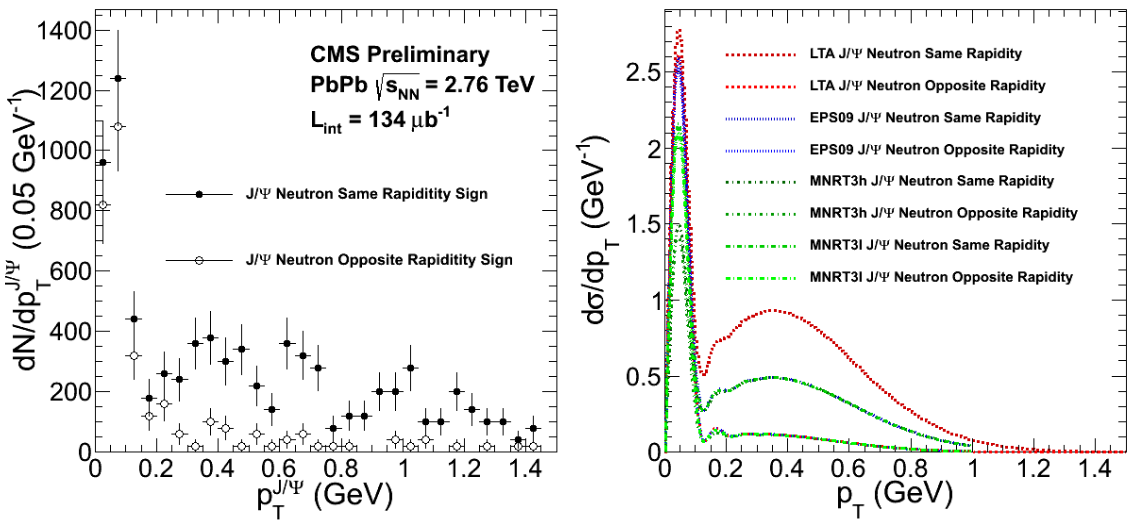

Figure 5.7: Transverse momentum distribution of the J/ψ when J/ψ and neutron have the same or opposite rapidity direction from data (left) and from theory (right).

tion to the neutron direction. The ratios, as described below are also given in the Tab. 5.4: $R^{y^+/y^-}_{ZDC^-}$: ratio between the number of J/ψ having $y > 0$ to the number of J/ψ having $y < 0$ from the events that fired ZDC$^-$

$R^{y^-/y^+}_{ZDC^+}$: ratio between the number of J/ψ having $y < 0$ to the number of J/ψ having $y > 0$ from the events that fired ZDC$^+$

Table 5.4: Final number of J/ψ (for both ZDCs and for two negative and positive rapidity) and ratios with statistical uncertainty.

	ZDC$^-$ $y < 0$	ZDC$^-$ $y > 0$	$R^{y^+/y^-}_{ZDC^-}$	ZDC$^+$ $y < 0$	ZDC$^+$ $y > 0$	$R^{y^-/y^+}_{ZDC^+}$
coherent J/ψ	63	68	1.08±0.19	42	69	0.61±0.12
incoherent J/ψ	141	26	0.184±0.039	13	111	0.117±0.034

The combined ratio $R^c_{opp/same}$ is calculated as

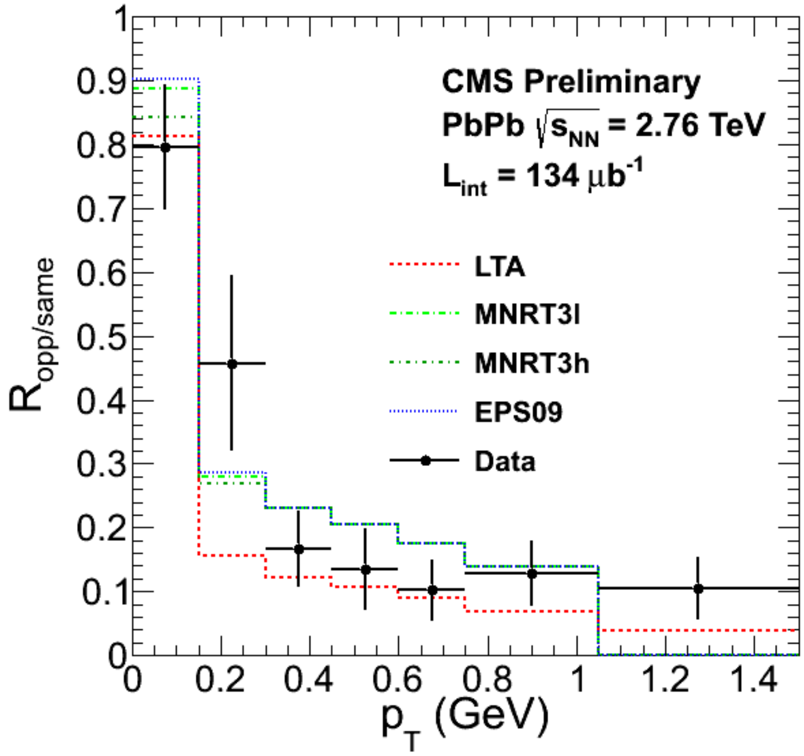

Figure 5.8: Ratio between the transverse momentum distribution of the J/ψ when J/ψ and neutron have the opposite direction and the transverse momentum distribution of the J/ψ when J/ψ and neutron have the same direction.

$$R^{c}_{opp/same} = \frac{ZDC^{-}\text{and } y > 0 + ZDC^{+}\text{and } y < 0}{ZDC^{-}\text{and } y < 0 + ZDC^{+}\text{and } y > 0}$$

- $R^{c}_{opp/same}$ for coherent J/ψ= 0.83 $\pm$ 0.12.
- $R^{c}_{opp/same}$ for incoherent J/ψ= 0.155 $\pm$ 0.021.

The correction factors (efficiency, reconstruction) are as following:

- $\varepsilon_{ZDC^{-}}$: efficiency of the ZDC^{-} of 0.98
- $\varepsilon_{ZDC^{+}}$: efficiency of the ZDC^{+} of 0.94

- ε_{μ^-}: efficiency $\times$ reconstruction of the muons with rapidly <0: 1.0
- ε_{μ^+}: efficiency $\times$ reconstruction of the muons with rapidly >0: 1.014.

The combined ratio $R^{ceff}_{opp/same}$ corrected with the factors above is calculated as

$$R^{ceff}_{opp/same} = \frac{\varepsilon_{ZDC^-}\varepsilon_{\mu^+}ZDC^-\text{and } y>0+\varepsilon_{ZDC^+}\varepsilon_{\mu^-}ZDC^+\text{and } y<0}{\varepsilon_{ZDC^-}\varepsilon_{\mu^-}ZDC^-\text{and } y<0+\varepsilon_{ZDC^+}\varepsilon_{\mu^+}ZDC^+\text{and } y>0}$$

$R^{ceff}_{opp/same}$ is 0.83± 0.12.

- $R^{ceff}_{opp/same}$ for coherent J/ψ= 0.83 ± 0.12.
- $R^{ceff}_{opp/same}$ for incoherent J/ψ= 0.154 ± 0.021.

If considering 3 significant figures for the representation of the result these values are:

- $R^{c}_{opp/same}$ for coherent J/ψ= 0.833 ± 0.124
- $R^{c}_{opp/same}$ for incoherent J/ψ= 0.155 ± 0.021
- $R^{ceff}_{opp/same}$ for coherent J/ψ= 0.828 ± 0.124
- $R^{ceff}_{opp/same}$ for incoherent J/ψ= 0.154 ± 0.021

This shows that in this measurement the efficiencies factors are negligible.

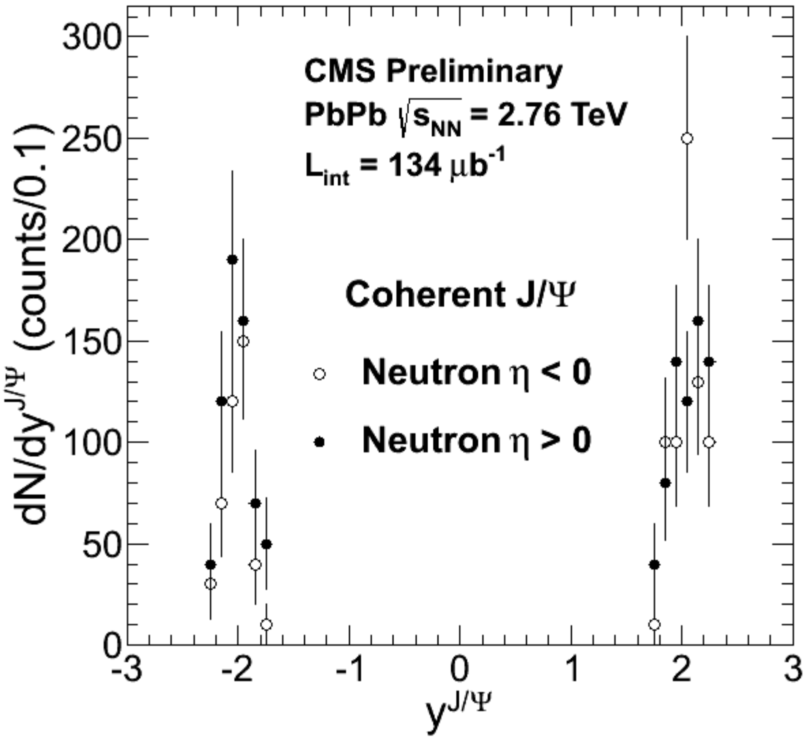

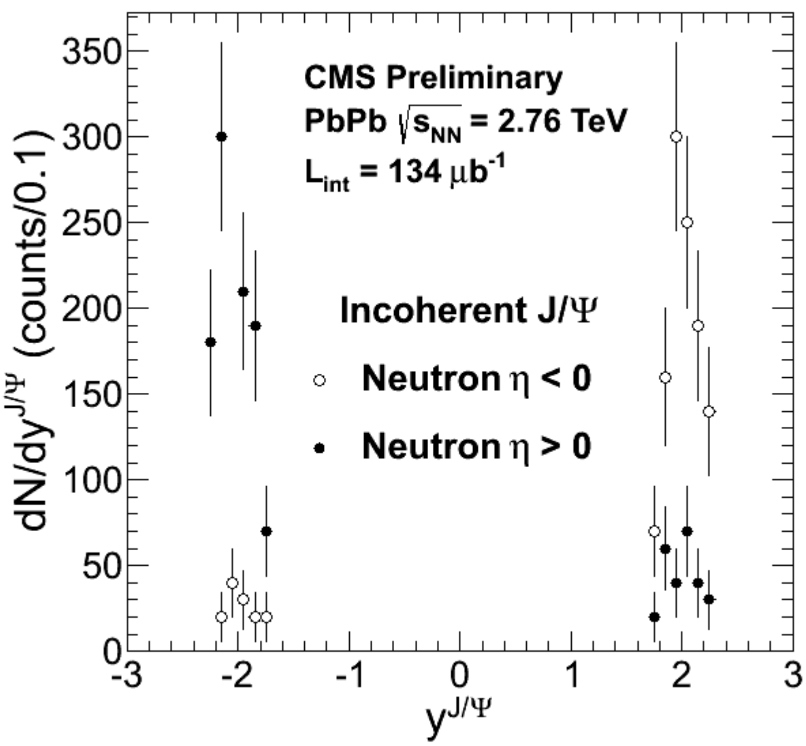

Figure 5.9: The rapidity distribution of the coherent (top) and incoherent (bottom) J/ψ for the ZDC$^+$ and ZDC$^-$.

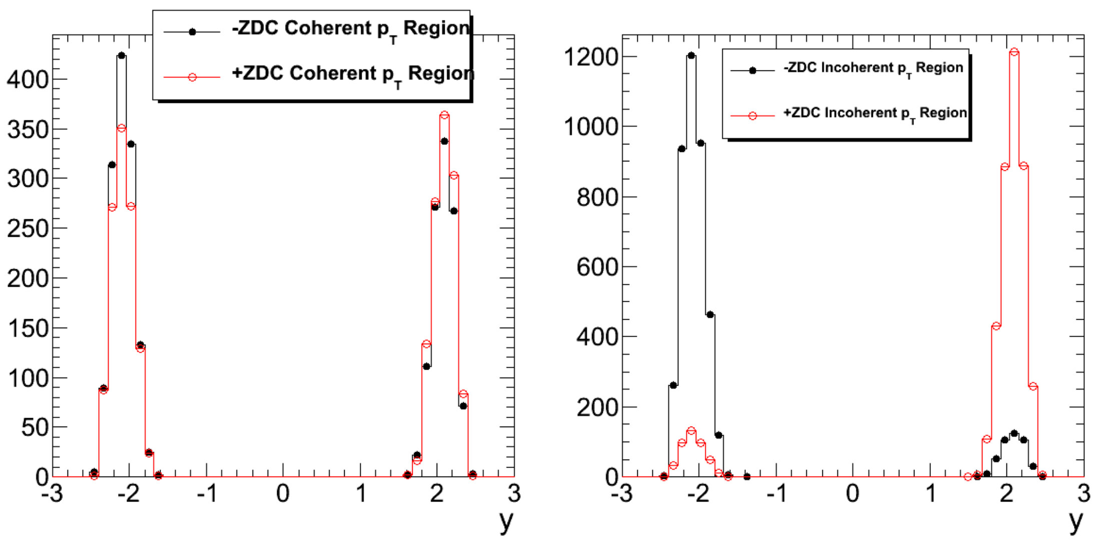

Figure 5.10: The rapidity distribution of the coherent (left) and incoherent (right) J/ψ for the ZDC$^+$ and ZDC$^-$ from MC (particle gun with customized $J/\psi p_T$ input distribution).

Chapter 6

Conclusion

6.1 xsection results

6.2 correlation results

Chapter 7

Future Works

7.1 Studies of 2011 PbPb data

7.1.1 High mass $\gamma - \gamma \rightarrow e^+e^-$ in PbPb 2011

A study of the di-electron production in UPC events is already possible from the recorded 2011 data. This measurement would make use of the electron triggers and combined the current di-muon data with di-electron data from the triggers using the ECAL. The electron triggered sample potentially offers a large increase in statistics. By adding the additional channel the statistics would already increase. However in addition to this, because of the smaller mass of the electron, di-electron production is slightly favor compared to di-muon production. STARlight predicts that di-electron cross section is a factor of more than 2.5 higher in Xn break-up mode than the di-muons channel when looking at masses above 4 GeV. The acceptance for electrons in potential higher as well. The ECAL is position just beyond the tracker, whereas the muon system is outermost sub-detector. This elevates the main reduction of muon acceptance, which is the material budget. There is simply a lot a detector in front the muon system.

In order to perform the study several key additions would need to be made relative to the current di-muon analysis. The original reconstruction of the data used in the current di-muon analysis does not contain electron objects. Either the analysis would have to migrated to reconstruction of the data done in a newer software version, or reconstruction of the electrons would have to be added to the current analysis chain. There are currently no electron UPC MC samples produced. In order to study the acceptance and efficiency for electrons these samples would be need. The ultimate limitation on this study is the 2 GeV threshold in p_T in the ECAL trigger. This limits the di-electron mass range to where the trigger is efficient.

The contribution of higher order diagrams can be explored by the photoproduction of di-lepton pairs is to explore. With additional contributions to the physics communities understanding of this process this study will help to determine necessity or non-necessity of including higher order of corrections in simulations such as STARlight. Having an additional channel to help constrain the current di-muon measure of the of UPC $\gamma-\gamma$ interaction will also help to constrain the J/ψ measurement by adding a data driven check on the normalization $\gamma-\gamma$ background to the J/ψ

7.1.2 UPC Hadronic Overlap and PbPb 2011

In the model calculations explored in this analysis of UPC quarkonia photoproduction all hadronic interactions are rejected. Photoproduction in events where hadronic interactions occur are not included in the cross section calculation. However, inclusive p_T spectra of J/ψ measured by ALICE in peripheral PbPb collisions show a low momentum peak consistent with coherent photoproduction [13]. CMS has the opportunity to explore this overlap between hadronic interactions and photoproduction using PbPb data from 2011 that is already recorded.

To study the overlap between photoproduction and hadronic proctuction of quarkonia event the inelastic sample and the UPC sample could both be used. The looseness of the veto designed to reject hadronic interactions, which uses the BSC detector, leaves a significant overlap with peripheral hadronic collisions. The inclusive quarkonia sample from typical hadronic collisions can also be utilized. Coherent quarkonia photoproduction has a distinctive low p_T structure that can be used to identify photoproduced candidates in a sample that contains photoproduction combined with hadronic interactions. This measurement would open up the door to exploring the boundary between photoproduction and hadronic production. By looking at the mixing of the two, both

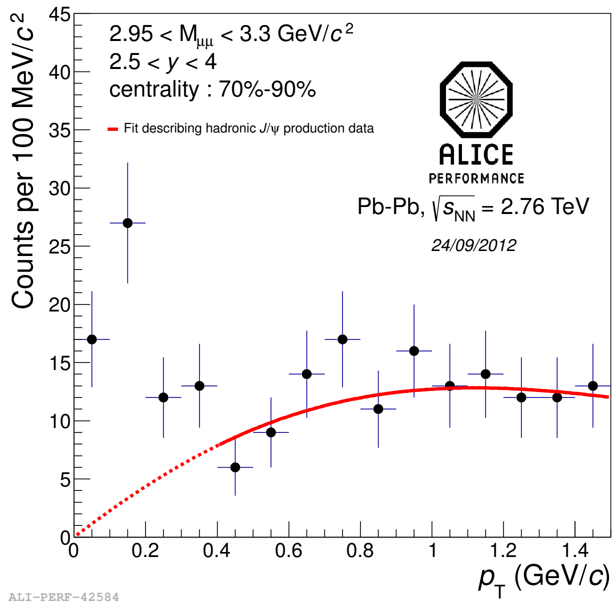

Figure 7.1: Coherent excess in inclusive J/ψ p_T spectrum.

process, hadronic production and photoproduction, will be better understood.

In order to compliment each others strengths, the inclusive hadronic sample and the UPC sample of dimuon candidates would be utilized in this study. The two samples muon and centrality biases are orthogonal allowing each to serve as a check on the other. The inclusive hadronic sample is triggered by a higher p_T threshold double trigger, whereas the UPC sample is uses a lower p_T single muon trigger. The UPC sample is strongly biased toward peripheral events, which would lead to inefficiencies as events become more central, whereas, the inclusive sample is slightly biases in the most peripheral events due to an inefficiency an event selection efficiency in the most peripheral centrality bin. If these offsetting biases can be exploited, clarity about the transition between and mixing of photoproduction and hadronic production of quarkonia can be produced. A measurement of the kind proposed here will both produce a better understanding of the low p_T portion of the inclusive spectrum as well as the hadronic overlap with UPC measurements.

7.1.3 UPC with muons in HF

As higher rapidities are explored both lower and higher momentum partons of the nucleus are probed. Because these two contributions to the UPC photoproduction cross section can be separated using neutron tagging in incoherent events, exploring higher dimuon rapidities becomes attractive. HF extends to 5 in η, 2.6 units beyond the edge of the tracker. By combining hits in HF with tracks in the tracker the higher dimuon rapidities could be explored. When combined with neutron tagging of incoherently produced quarkonia, the current study can be extended to probe lower-x nuclear partons by identifying muons in HF.

7.2 Studies of 2013 pPb data and 2015 PbPb data

Specific UPC triggers were also developed for the pPb run in 2013. For this period of running a much higher total trigger rate was read out relative to 2011. The total rate allocated for UPC triggers at the L1 in 2013 was 5kHz and 50 Hz at the HLT. This factor of 5 increase in the bandwidth, especial in L1 rate, allowed for a different triggering strategy than in 2011.

The basic strategy in 2013 was the same as in 2012, use the loosest available ECAL and muon L1 triggers to push to capture the lowest p_T electrons and muons possible and veto on hadronic interactions, but was impemented differently. Because of the L1 bandwidth restrictions in 2011, both the ZDC and the BCS were used on the L1 to reduce rates. In 2013 only the muon and ECAL triggers were used on the L1 allowing for rejection of hadronic interactions through cuts on track multiplicity. In addition, a more sophisticated trigger using full dimuon reconstructed was developed to increase purity. The main advantage in this shift in strategy was a higher purity due to the increased sophistication of the reconstruction on the HLT. In addition, an increase in cross section of the underlying physics process was achieved by relaxing the neutron emission requirement.

The HLT triggers in 2013 rejected hadronic interactions through counting tracks. For the five UPC trigger paths included in the HLT meanu, three levels of reconstruction were done at the HLT.

Pixel tracks were reconstructed from the inner pixel section of the silicone tracker alone, tracks were reconstructed using the full tracker using the strips as well, and full dimuon reconstruction was done using the tracker and muon detector. The least restrictive pixel track paths required at least one track reconstructed from the pixel detector and less than 10 pixel tracks in the event. Full tracking paths were added on top of the pixel track paths and included an additional requirement of one full track and less than 7 reconstructed tracks. The most restrictive path added to the pixel and full tracking paths and required reconstruction of dimuons with a mass between 2 and 10 GeV. The design of these triggers allowed for higher signal purity relative to 2012 through use of full tracking on the HLT and allowed for increased exposure to the cross section by removing the break-up requirement implicit in requiring a ZDC trigger on the L1.

The PbPb run in 2015 will be at higher beam energies and luminosities. The $sqrts_{NN}$ will increase from 2.76 TeV in 2011 to 5.1 TeV with a project integrated luminosity between $0.3/nb$ and $1/nb$. The factor of 2 to 10 increase in integrated luminosity will increases the number of events directly. In addition, both the increase in energy, which increases the photon flux, and the ability to utilize the 2013 trigger strategy of sifting the onus of the trigger selection to the HLT will increase the measured yields relative to 2011. The higher beam energy, higher integrated luminosity, and added selectivity of the HLT will create the opportunity to explore both J/ψ with greater statistical precision and novel objects such as Υ, and jets.

7.2.1 pPb J/ψ

J/ψ photoproduciton in pPb collisions is dominated $\gamma - p$ interactions. The measurement would primarily probe the proton gluon densities. In Eq. 2.13 the photon flux depends on the square of the number of protons in parent nucleus, Z^2. However, the cross section of the target only increase as the total number of nucleons to the 2/3rds power, $A^{2/3}$. The much higher photon flux from the Pb ion more than compensates for the decreased size of the proton.

A pPb UPC J/ψ measurement will compliment the measurements done at HERA, and measurements done by ALICE. CMS will contribute by adding additional kinematic coverage and cover a unique range of proton-photon center of mass energies, $W_{p\gamma}$. The difference in beam energies and species at LHC versus HERA result in access to different $W_{p\gamma}$. ALICE and CMS have different acceptance in J/ψ rapidity, which also translates to coverage of different $W_{p\gamma}$. In addition, an excess in the UPC cross section compared to HERA measurements would indicate a non-exclusive contribution to the pPb UPC J/ψ cross section. This measurement will both help enhance the current understanding of the $p\gamma$ J/ψ photoproduction cross section as a function of $W_{p\gamma}$, and validate the UPCs measurements as an extension of the work done at HERA.

7.2.2 UPC J/ψ and Υ in 2015

A measurement of the UPC J/ψ in 2015 will produce a strong constraint on the low-x portion of the nuclear gluon distribution relative to the current analysis form the 2011 data. The J/ψ measurement will probe lower-x than in 2011 due to the increase in beam energy. A measurement in 2015 will also have lower statistical errors due to the increase in integrated luminosity and increased L1 bandwidth. UPC J/ψs in 2015 will push farther towards the onset of low-x parton saturation.

Measurement of the UPC Υ cross section from the 2015 data will be the first from PbPb collisions. As with the J/ψ, Additional L1 bandwidth, increased beam energy, and and intensity will increase the Υ yield significantly relative to 2011. The acceptance for Υ is near 40% for all rapidities between -2.4 to 2.4 (see Fig 7.2). Conversely, J/ψ acceptance is 8% near 2 in dimuon rapidity only. Below 1.6 in rapidity there is not acceptance for for UPC J/ψ. Estimates from STARlight predict a factor of 17-60 increase in yield depending on the total delivered integrated luminosity. The Υ measurement will be a new measurement that will expand the range of x and Q^2 probed with a higher energy probe that is better suited to the acceptance of CMS.

7.2.3 UPC jets

Like Υs, UPC photoproduction of jets is a novel probe. The LHC 2015 heavy ion run presents an opportunity do this measurement for the first time. The cross section for photoproduction of

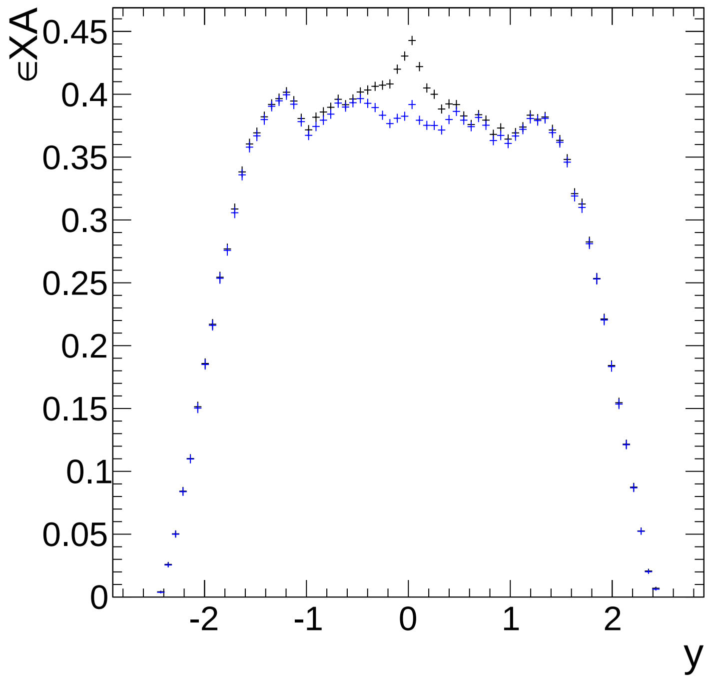

Figure 7.2: υ efficiency times acceptance in CMS from STARlight for $\sqrt{s_{NN}} = 5.1$ TeV as function of y.

jets was estimated in Ref [**?**] and found $b\bar{b}$ and $c\bar{c}$ on the order of 1 mb and 1b respectively. With the integrated luminosity expected for 2015 as many as $1x10^6$ $b\bar{b}$ events and $1x10^9$ $c\bar{c}$ events. Jet photoproduction is not constrained by the mass of the bound onia states like in J/ψ and Υ photoproduction. For this reason, jet photoproduction probes a wider range of x and Q^2. UPC jets therefore will both expand on the J/ψ and Υ measurements in addition to providing an additional validating compliment to the onia measurements.

The jet measurement will require additional trigger development and analysis design. The jet signal differs significantly from the dimuon signals used in the current analysis. The trigger scheme used in the 2013 pPb run selected UPC events by vetoing events with high numbers of track. The track multiplicity of the jets will not pass this requirement. However, new L1 trigger logic is currently being developed to separate the jet from the underlaying event in nuclear collisions. This trigger logic could also be utilized to select jet events that produce very little to no underlaying event. In addition to the trigger, jet reconstruction algorithms would needed to be adapted to push

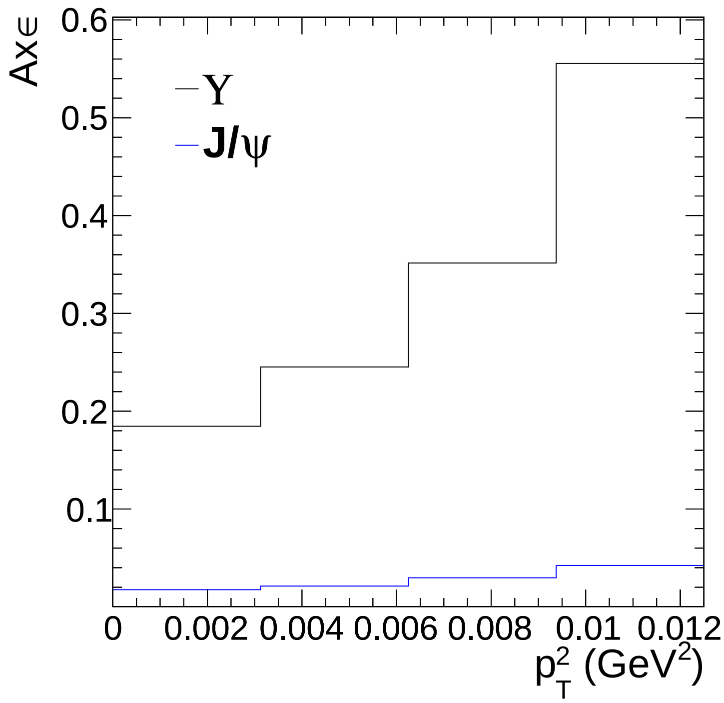

Figure 7.3: Comparison of υ and J/ψ efficiency times acceptance in CMS from STARlight for $\sqrt{s_{NN}}$ = 5.1 TeV as function of p_T.

to the lower pT jets they are produced by photoproduction. The UPC jet measurement will demand extra preparation compared to the onia measurements, but the development will overlap with many of the goals that are already being pursued by the CMS Heavy Ion group and will allow for wider collaboration.

References

[1] S. Chatrchyan *et al.*, “The cms experiment at the cern lhc,” *Journal of Instrumentation* **3** no. 08, (2008) S08004. `http://stacks.iop.org/1748-0221/3/i=08/a=S08004`.

[2] **PHENIX Collaboration** Collaboration, A. Adare *et al.*, “Cold Nuclear Matter Effects on J/ψ Yields as a Function of Rapidity and Nuclear Geometry in Deuteron-Gold Collisions at $\sqrt{s_{NN}} = 200$ GeV,” *Phys.Rev.Lett.* **107** (2011) 142301, `arXiv:1010.1246 [nucl-ex]`.

[3] J. D. Jackson, *Classical electrodynamics*. Wiley, New York, NY, 3rd ed. ed., 1999. `http://cdsweb.cern.ch/record/490457`.

[4] E. Fermi, “On the Theory of Collisions between Atoms and Electrically Charged Particles,” in *Electromagnetic Probes of Fundamental Physics*, W. Marciano and S. White, eds., pp. 243–252. Sept., 2003. `hep-th/0205086`.

[5] C. A. Brau, *Modern Problems in Classical Electrodynamics*. Oxford, New York, NY, 1st ed. ed., 2004.

[6] S. R. Klein and J. Nystrand, “Exclusive vector meson production in relativistic heavy ion collisions,” *Phys. Rev. C* **60** (Jun, 1999) 014903. `http://link.aps.org/doi/10.1103/PhysRevC.60.014903`.

[7] V. Rebyakova, M. Strikman, and M. Zhalov, “Coherent rho and J/psi photoproduction in ultraperipheral processes with electromagnetic dissociation of heavy ions at RHIC and LHC,” *Phys.Lett.* **B710** (2012) 647–653, `arXiv:1109.0737 [hep-ph]`.

[8] V. Rebyakova, M. Strikman, and M. Zhalov, “Coherent ρ and J/Ψ photoproduction in ultraperipheral processes with electromagnetic dissociation of heavy ions at RHIC and LHC,” *Physics Letters B* **710** no. 4–5, (2012) 647 – 653. http://www.sciencedirect.com/science/article/pii/S0370269312003152.

[9] A. Adeluyi and C. A. Bertulani, “Gluon distributions in nuclei probed at energies available at the CERN large hadron collider,” *Phys. Rev. C* **84** (Aug, 2011) 024916. http://link.aps.org/doi/10.1103/PhysRevC.84.024916.

[10] A. Adeluyi and T. Nguyen, “Coherent photoproduction of ψ and Υ mesons in ultraperipheral pPb and PbPb collisions at the CERN Large Hadron Collider at $\sqrt{S_{NN}} = 5$ TeV and $\sqrt{S_{NN}} = 2.76$ TeV,” *Phys. Rev. C* **87** (Feb, 2013) 027901, arXiv:1302.4288 [nucl-th]. http://link.aps.org/doi/10.1103/PhysRevC.87.027901.

[11] **ALICE** Collaboration, B. Abelev *et al.*, “Coherent J/ψ photoproduction in ultra-peripheral Pb-Pb collisions at $\sqrt{s_{NN}} = 2.76$ TeV,” *Physics Letters B* **718** no. 4–5, (2013) 1273 – 1283. http://www.sciencedirect.com/science/article/pii/S0370269312012257.

[12] V. Guzey, E. Kryshen, M. Strikman, and M. Zhalov, “Evidence for nuclear gluon shadowing from the ALICE measurements of pbpb ultraperipheral exclusive production,” *Physics Letters B* **726** no. 1–3, (2013) 290 – 295. http://www.sciencedirect.com/science/article/pii/S0370269313006825.

[13] A. Lardeux, “J/ψ production in Pb-Pb collisions at $\sqrt{s_{NN}}$ =2.76 TeV in the ALICE experiment,” *J.Phys.Conf.Ser.* **446** (2013) 012042.

Appendix A

My Appendix, Next to my Spleen

There could be lots of stuff here